ANALYSIS OF A CIRCULAR COMPOSITE DISK SUBJECTED TO EDGE ROTATIONS AND HYDROSTATIC PRESSURE

by

STANLEY T. OLIVER

A THESIS

Submitted in partial fulfillment of the requirements
of the degree of Master of Science
of
The School of Mechanical and Aerospace Engineering
of
The University of Alabama in Huntsville

HUNTSVILLE, ALABAMA

2004

In presenting this thesis in partial fulfillment of the requirements for a master's degree from The University of Alabama in Huntsville, I agree that the Library of this University shall make it freely available for inspection. I further agree that permission for extensive copying of scholarly purposes may be granted by my advisor or, in his/her absence, by the Chair of the Department (Director of Program) or the Dean of the School of Graduate Studies. It is also understood that due recognition shall be given to me and to The University of Alabama in Huntsville in any scholarly use which may be made of any material in this thesis.

_____ _____

(student signature) (date)

THESIS APPROVAL FORM

Submitted by Stanley Oliver in partial fulfillment of the requirements for the degree of Master of Science in Engineering in Mechanical and Aerospace Engineering and accepted on behalf of the Faculty of the School of Graduate Studies by the thesis committee.

We, the undersigned members of the Graduate Faculty of The University of Alabama in Huntsville, certify that we have advised and/or supervised the candidate on the work described in this thesis. We further certify that we have reviewed the thesis manuscript and approve it in partial fulfillment of the requirements of the degree of Master of Science in Mechanical and Aerospace Engineering.

_____ Committee Chair
(Date)

_____

_____

_____ Department Chair

_____ College Dean

_____ Graduate Dean

Abstract

The structural analysis results for a graphite/epoxy quasi-isotropic circular plate subjected to a forced rotation at the boundary and pressure is presented. The analysis is to support a specialized material characterization test for composite cryogenic tanks. Finite element models were used to ensure panel integrity and determine the pressure necessary to achieve a predetermined equal biaxial strain value. The displacement results due to the forced rotation at the boundary led to a detailed study of the bending stiffness matrix [D]. The variation of the bending stiffness terms as a function of angular position is presented graphically, as well as, an illustrative technique of considering the laminate as an I-beam.

ACKNOWLEDGEMENTS

The work described in this thesis.....

TABLE OF CONTENTS

LIST OF FIGURES

LIST OF TABLES

LIST OF SYMBOLS

General Abbreviations

[A]	laminate extensional stiffness matrix
[B]	laminate bending-stretching coupling matrix
[D]	laminate bending stiffness matrix
E	Young's modulus - isotropic
E1, E2, E3	axial moduli - principal material directions
Ex	axial modulus
Ey	transverse modulus
G	shear modulus - isotropic
[M]	moments per unit length
[N]	in-plane forces per unit length
[Q]	reduced stiffness
[R]	Reuter matrix
[T]	transformation matrix
x,y	structural axes
x,y,z	global coordinates
1,2,3	material principal coordinates
CBPA	Cryogenic Biaxial Permeability Apparatus
CLT	Classical Lamination Theory
CTE	coefficient of thermal expansion
Gr/Ep	graphite/epoxy
F°	degree Fahrenheit
LH2	liquid hydrogen
MSFC	Marshall Space Flight Center
NASTRAN	NASA Structural Analysis
NASA	National Aeronautics and Space Administration

a	distance from center to outer edge of circular plate
b	radial position
P	concentrated load
r	radial position
z	upward normal of plate
q_o	distributed pressure
in	inch
psi	pound force per square inch
msi	one million pound force per square inch = $1*10^6$ psi
ksi	one thousand pound force per square inch = $1*10^3$ psi
lbf	pound force
z	plate normal direction

Chapter 1

INTRODUCTION

1.1 Background

Some near future goals for the space industry are to develop safe and reliable launch vehicles, reduce risk, and to reduce the cost of launching a payload. To achieve these goals, the next generation of space launch vehicles must be more weight efficient. One potential weight saving measure is to utilize composite materials for primary structures.

Propellant tanks make up a large percentage of the dry weight of a launch vehicle. Utilizing composites for propellant tanks provides several advantages; a potential weight reduction due to a lower density than aluminum, higher strength, and the stiffness can be tailored to meet specific loading profiles. However, composites also present many manufacturing and performance obstacles that currently prohibit their use in large cryogenic tanks. The size of tooling, excessive exposure time of pre-impregnated material during fabrication, the availability of a large diameter autoclave, etc., are just a few of the manufacturing difficulties. The performance of composites in a cryogenic environment requires numerous tests to verify the stiffness, strength and integrity of the material. The degradation of the matrix material when subjected to cyclic, cryogenic temperatures is also of great concern.

Microcracks are a form of matrix material degradation. Microcracks are microscopic cracks in the matrix material caused by excessive mechanical strain, and can also occur due to excessive thermal strain being developed due to differences in the coefficients of thermal expansion (CTE) of fibers and matrix. Since microcracking can

be caused by extreme temperature alone, the use of composite materials for a cryogenic tank must be thoroughly evaluated.

A consequence of matrix microcracking is permeability. Permeability is the slow leaking of gas through a material, or in this case a laminate. If a sufficient number of microcracks develop within each ply of a laminate, a network of cracks can serve as a pathway for gas to permeate through the laminate.

Microcracking and permeability phenomena led to a test program to qualify materials for cryogenic tank usage based on their resistance to microcracking and permeability. A reliable test would be a full-scale tank, yet the costs associated with such a test, as well as, the inability to test many material systems, make this option too costly. Small pressurized filament-wound bottles provide a biaxial strain field, but the pressures required to generate the same flight strain will be very high and could influence the permeability through the walls of the vessel. The test should closely simulate a pressure vessel in service, simulating a flight profile, cycling pressure and temperature to develop a knowledge base for full-scale development and screening potential materials under similar environments expected in flight.

1.2 Cryogenic Biaxial Permeability Apparatus

The Cryogenic Biaxial Permeability Apparatus, CBPA, developed and utilized by Marshall Space Flight Center is a test apparatus consisting of a flat, circular composite laminated plate that uses pressure to develop strain and liquid hydrogen for the thermal environment. The pressurized circular plate develops a biaxial strain field in the plate. In the center of the plate, the strain field is equal-biaxial. It is in this region where hydrogen

permeability is measured. This test apparatus allows for material characterization or performance evaluation under combined thermal-mechanical environments that simulate flight conditions. This test has the advantage of providing a large diameter, equal-biaxial strain level and maintaining a liquid hydrogen interface in intimate contact with the inner surface of the laminate. In Figure 1.1, a cross section of the apparatus is shown. In this representation, the panel has been pressurized hydrostatically and deforms into a dome shape. The two Invar rings hold the specimen and the two Invar rings are bolted to the stainless steel bucket.

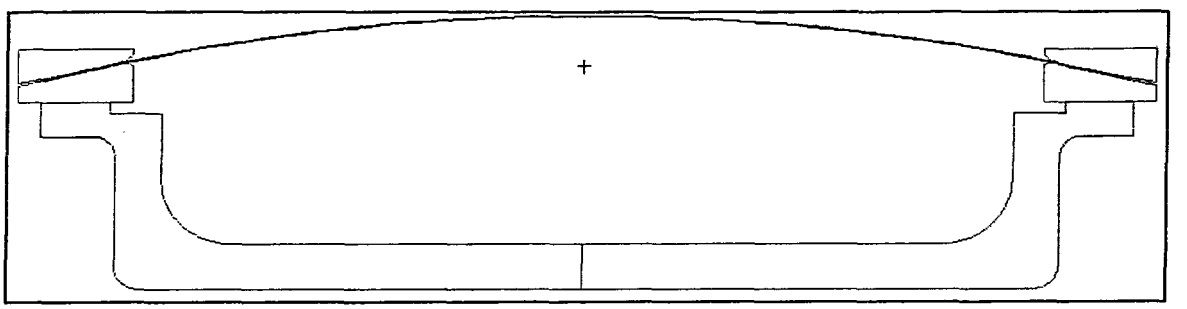

Figure 1.1 A cross section of the CBPA.

1.2.1 CBPA Test

The objective of the test was to determine candidate materials for a reusable composite cryogenic tank by measuring hydrogen permeability of a composite panel subjected to a cyclic cryogenic environment and strain level [9]. The strain level chosen was considered to be sufficiently severe to initiate microcracking of the matrix material. The number of cryogenic cycles was thought to be sufficient to allow all microcracking and redistribution of load to occur, thus progressive damage would stabilize. Embedded within each cryogenic cycle was five pressurization cycles. Combined, the strain levels, cryogenic cycles and pressure cycles of the test sequence would allow separation within the permeability test data to distinguish and rank candidate materials for a reusable

composite cryogenic tank. For standardization, it was planned that each panel design used the same ply thickness, panel thickness, and stacking sequence and each candidate material was subjected to the same test sequence.

A cryogenic cycle took several hours to complete. The cryogenic cycle consisted of a room temperature composite panel being chilled to a cryogenic temperature and maintaining the temperature until a steady-state cryogenic condition was achieved. During the steady-state cryogenic condition, multiple pressure cycles were applied that produced the desired strain levels in the center of the composite panel and permeability measurements are taken during each pressure cycle. Then the composite panel is returned to room temperature to complete one full cryogenic cycle. A full test sequence is five cryogenic cycles with 25 pressure cycles embedded.

1.2.2 CBPA Design

The design of the test apparatus had the benefits of quickly introducing a consistent biaxial strain field, thoroughly soaking the test panel in cryogenic liquid, and measuring hydrogen permeability in-situ. This approach eliminated the concern of under-strained transverse plys as found in uniaxial tests. It also eliminated any uncertainty of temperatures at the face of the composite panel.

The initial design of the CPBA had the thin composite panel clamped between two Invar rings. Invar was chosen instead of steel or aluminum because it has a CTE in the range of typical composites. Figure 1.2 is a schematic of the pre-assembly configuration. The inside and outside Invar rings and their opposing taper angle are shown. The composite panel is placed on the lower ring and epoxy is applied to the

upper ring. The system is clamped together and allowed to cure prior to attaching to the stainless steel bucket.

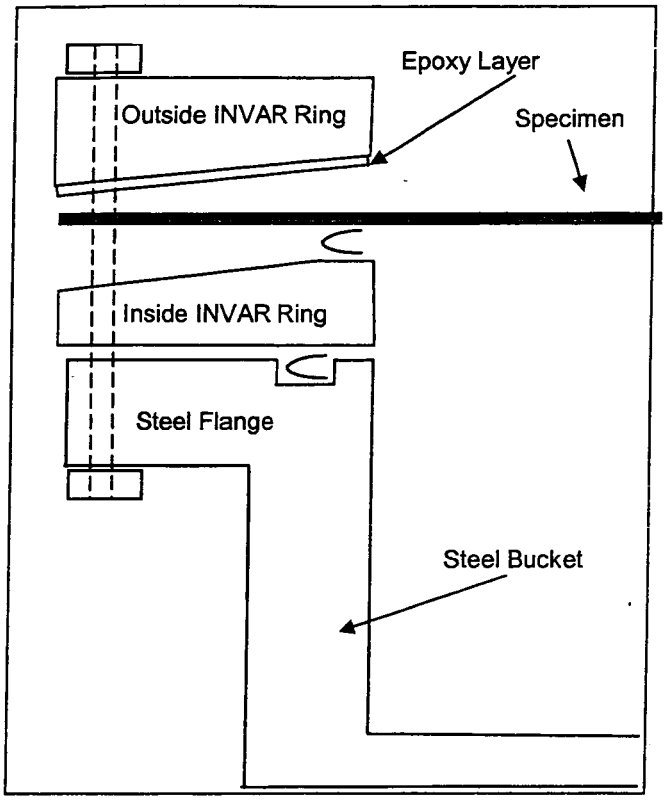

Figure 1.2 Schematic of the pre-assembly configuration.

Sparks [9] provides the final dimensions of the CBPA deign. The outside diameter of the Invar rings and composite panel is twenty-five inches. The inside diameter of the Invar rings is twenty inches, thus a two inch wide clamped region is provided around the periphery. Sixty equally spaced fasteners at a bolt circle of 22.50 inches clamp together the upper Invar ring, the composite panel, the lower Invar ring and a stainless steel bucket that contains the pressurized cryogen. An adhesive is applied between the composite plate and upper Invar ring and remains uncured during the clamping. Provisions are made to prevent leakage between the interfaces. The entire system is inverted during

testing to ensure the cryogen is in intimate contact with the composite panel. The design assumes the two invar rings and the composite plate are free to move radially as a system. The relative motion, due to the CTE mismatch of the steel and Invar/composite system, is allowed between the Invar/composite system and the stainless steel tub.

1.3 Objective

The objective of this thesis is to investigate the structural behavior of a circular graphite/epoxy laminate (plate) subjected to a pressurized cryogenic environment and induced loads from applied boundary conditions. The analysis utilizes a nonlinear finite element solution technique to address the large out of plane displacement. The inspiration for this thesis study is the response of the panel during the bonding process, or assembly of the panel to the two rings. The enforced displacement and rotation at the boundary bends the panel near the edge. The finite element analysis of the assembly procedure produced an unexpected displacement field in which the out-of-plane displacements are not uniform like a dome, but vary with both radius and tangential location. The out-of-plane displacement field appears to be orthogonal, but is not aligned with the material or global coordinate system.

Chapter 2

LITERATURE REVIEW

2.1 Introduction

This thesis investigates the structural behavior of a circular, composite test specimen utilized in a specialized permeability test for materials characterization. A review of test methods previously used to investigate microcracking and/or permeability of composite materials provide a history of some important tests. In general, these tests strain a composite laminate sufficiently to develop mechanically induced microcracks; however, most permeability test did not subject a specimen to liquid hydrogen. In addition, a structural test to generate equal-biaxial strain for small composite disks provided additional insight into laminate behavior. The theory of mechanics of composite materials is an important subject with respect to this work. This information provides the background theory necessary to develop the methodologies for analyzing composite materials. Other literatures of composite materials specialize in specific areas of composite design and analysis, highlighting the structural properties of laminates. Finite element models were used to develop some of the results presented in this thesis. Literature supporting the convergence and validation of finite element models were reviewed.

2.2 Test Methods

The NASA X-33 Failure Report [12] discusses the Liquid Hydrogen (LH2) tank failure in detail, presenting the most probable cause of the failure and the test methods used to verify the findings. The investigation determined that the infiltration of gaseous hydrogen into the cells of the honeycomb core and the warming of the tank after draining

resulted in high pressures within the core, which caused separation of the facesheet from the core. The X-33 failure investigation brought the issue of microcracking of composite cryogenic tanks to a new level of importance. [12]

Southern Research Institute performed permeability testing on facesheet material excised from various acreage locations of the X-33 LH2 tank. [12] Two tests were designed for these samples. They combine flight level in-plane strain and reduced temperature to load the samples. The permeability of the samples was measured under these loads. A 12-inch diameter panel was slit radially at eight locations creating eight pull-tabs which were linked to an octagonal load frame, which provided the mechanism for introducing the mechanical load. The design of the test apparatus did not allow permeability to be measured while the specimen was mechanically and thermally loaded. A restraining ring had to be installed in an attempt to maintain the required strain level. The panel and restraining ring had to be moved to the permeability testing facility. An improvement in the maintaining the desired strain level was utilized in the nine-inch diameter test. It had twenty-four load introduction tabs and a hydraulic mechanism for introducing the biaxial load through a compression ring grip.

Grimsley [5] is a post X-33 failure report that investigates possible solutions to solve the permeability issue, in particular, the usage of films and liners to act as a barrier to permeability. The test determined the permeance of argon at room temperature through a composite. Within the future work section of Grimsley's article, a very important statement was made, "Permeation at cryogenic temperatures need to be evaluated under an applied load to simulate flight conditions." [5]

Cavallaro et al. [5] evaluate the biaxial strain field of a composite disk by the finite element method and closed form analytical methods. The disk is quite small, a diameter of 50.8mm and a thickness of 2.25mm. The specimen is loaded using opposing concentric rings producing the biaxial strain field. An interesting section of the paper contains the calculations and variations of flexure moduli of several cross-ply laminates.

Sparks [9] provides a summary of all aspects involved in the CBPA, from the rationale for performing the test to the ranking of the material systems based on propensity to permeate hydrogen. He introduces the background and objectives of the test and provides a description of the test apparatus, including some design iterations involved in eliminating panel slippage. In addition, the permeability measurement technique and the details of the data acquisition are discussed. Spark's report summarizes the testing results for twenty-four panels subjected to a predefined test procedure involving thermomechanical cycling. Mechanical coupons were excised from each panel as well as microcrack density specimens. The Conclusions and Recommendations listed in Sparks highlight the successes of the permeability test program.

2.3 Mechanics of Composites

Literature reviewed to support the development of the theoretical background section was primarily Jones [6]. His text provided the theoretical background for stress-strain relations for orthotropic materials, stress-strain transformation of arbitrary orientations and the macromechanical behavior of a laminate based on classical lamination theory. The development of the laminate extensional, coupling and in

particular, the bending stiffnesses is an important concept associated with this thesis. Bower [2] provides insight into the mechanics of composites as well. Specifically, his text provides alternate expressions for the laminate stiffnesses, in particular, the bending stiffness. In addition, Bower derives a complete system of coupled simultaneously partial differential equations for the displacement of a laminate and provides simplifications based on the type of loading conditions encountered.

Tsai [11] begins his book similar to most popular textbooks by introducing the stress-strain relations using generalized Hooke's Law and showing the stiffness matrices of various material symmetries. The stiffness matrix of a unidirectional ply and the stress and strain transformation is followed by the comparison of elastic properties of common composite materials. Following the introduction to composite materials and their elastic properties, his book transitions to a unique presentation of in-plane and flexural stiffness characteristics. He shows graphically and through examples the transformation of elastic moduli as a function of ply angle for various materials. His presentation of polar plots of in-plane and flexural moduli as functions of the reference coordinate system support the finding of this thesis presented in Chapter 5. Specific laminates are presented in which the in-plane and flexural moduli exhibit isotropic, orthotropic, or anisotropic behavior.

The objective of Bailey's [1] dissertation was to derive the plate equations for a circular plate with orthogonal anisotropy. She presents the six stiffness terms of the bending stiffness matrix in terms of invariants. The results of these equations are compared with the results from this thesis.

2.4 Finite Element Model Convergence

The question of accuracy of finite element model results, especially for a complex model such as the one used in this thesis, is a difficult question to answer. Convergence and validation studies can provide reassurance that the model can predict accurate results. Spyrakos does not provide any general procedure that can be used to perform a convergence study. However, he does point out that the convergence of stresses is slower than the convergence of displacements. [10] Therefore, convergence based on stresses is used for this thesis. Comparing the finite element solution to a known analytical solution provides a qualitative assessment of the finite element model's behavior and provides confidence the model can predict acceptable results.

McKenney [7] compares the finite element method codes that use h version and p version, that differ on the element shape functions employed. [7] He investigates the potential time savings using a post-processing technique of a prescribed convergence criterion relative to stress. He presents a method of convergence for the h version elements based on mesh refinement, which is increasing the number of elements in a region of the model. The convergence criterion defined by McKenney for the h version elements is $\Delta\sigma/\Delta$DOF to be less than 0.10 psi/degree of freedom (DOF). This thesis uses h version elements and will base convergence on the same criterion.

Finite element model confidence studies can easily be accomplished for a model of circular geometry. There are numerous examples of various loading and boundary conditions that can provide an analytical basis to compare finite element model results. In particular, Cook [4] provides analytical solutions to isotropic plates subjected to concentrated and distributed loads and typical boundary conditions that are either fixed or

simply supported. [4] Important structural responses, such as displacement in the center or out-of-plane moments near the edge are presented.

Chapter 3

BACKGROUND THEORY

3.1 Introduction

The background section presents the two-dimensional, plane stress theory of composite material analysis. A single ply or lamina is defined by Jones [6] as "a flat arrangement of unidirectional fibers or woven fibers in a matrix." A laminate is a stack of individual laminae of various orientations. The macromechanical behavior of individual lamina is used to predict the structural response of the lamina to the various applied loads. The macromechanical behavior of laminates predicts the response of a laminate, which is also called the Classical Lamination Theory. The objective of composite design is to identify the material properties of both the lamina and laminate. The theory allows the behavior of any laminate to be predicted from a few material constants for the lamina.

3.2 Lamina Mechanics

The lamina mechanics theory assumes a linear-elastic response of a thin orthotropic lamina and also assumes the lamina is under plane stress due to the lamina thickness being much less than the in-plane dimensions. Lamina mechanics or the macromechanical behavior of lamina is used to predict the response of a lamina to loads that are not aligned with the principal material directions. Specifically, the objective is to write the stress-strain relationship in the global coordinate system with the stiffness

expressed as functions of the lamina mechanical properties and the orientation angle of the lamina.

For this study, the lamina consists of unidirectional fibers in a matrix, also known as tape. The longitudinal direction of the tape material, which is parallel to the fibers, is the first principal material direction, designated the 1-axis. The transverse direction or second principal material direction is designated the 2-axis. The moduli of elasticity in the principal material directions are E_1 and E_2. The shear modulus is G_{12} in the principal material direction and the Poisson's ratios in the principal material directions are ν_{12} and ν_{21}. This two-dimensional theory relates the lamina stresses, σ, to the lamina strains, ε, by

$$\begin{Bmatrix} \sigma_1 \\ \sigma_2 \\ \tau_{12} \end{Bmatrix} = [Q] \begin{Bmatrix} \varepsilon_1 \\ \varepsilon_2 \\ \gamma_{12} \end{Bmatrix}, \tag{3.1}$$

where [Q] is the reduced stiffness matrix involving the material engineering constants of the lamina, E_1, E_2, G_{12}, ν_{12} and ν_{21}. (Note: The List of Symbols, at the front of the document, presents the definitions of the various symbols used throughout this work.) The reduced stiffness matrix in terms of the engineering constants is:

$$[Q] = \begin{bmatrix} \dfrac{E_1}{1-\nu_{12}\nu_{21}} & \dfrac{\nu_{21}E_1}{1-\nu_{12}\nu_{21}} & 0 \\ \dfrac{\nu_{12}E_2}{1-\nu_{12}\nu_{21}} & \dfrac{E_2}{1-\nu_{12}\nu_{21}} & 0 \\ 0 & 0 & G_{12} \end{bmatrix}. \tag{3.2}$$

It is important to define the stress-strain relationship for a lamina of an arbitrary orientation to relate the stresses in the principal material axes, with respect to stresses in the global coordinate system. Figure 3.1 shows the global, x-y, coordinate system and

the principal material coordinate system, 1-2, aligned with the fibers of the lamina. Note

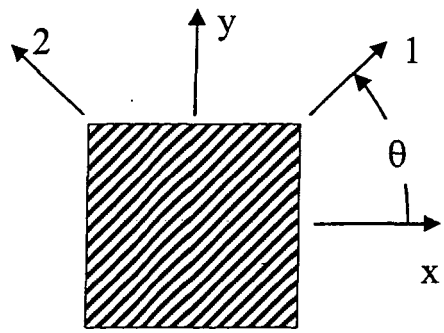

that in this figure, the positive z-direction is out of the page. The angle θ is the angle

Figure 3.1 Lamina coordinate system relative to structural coordinate system.

measured from the global X-axis to the principal material 1-axis made by a positive rotation about the Z-axis. The two-dimensional stress transformation matrix is

$$[T]=\begin{bmatrix} \cos^2\theta & \sin^2\theta & 2\sin\theta\cos\theta \\ \sin^2\theta & \cos^2\theta & -2\sin\theta\cos\theta \\ -\sin\theta\cos\theta & \cos\theta\sin\theta & \cos^2\theta-\sin^2\theta \end{bmatrix}, \tag{3.3}$$

and the transformation of stress from one coordinate system to the other is

$$\begin{Bmatrix} \sigma_1 \\ \sigma_1 \\ \tau_{12} \end{Bmatrix} = [T]\begin{Bmatrix} \sigma_x \\ \sigma_y \\ \tau_{xy} \end{Bmatrix} \quad \text{or} \quad \begin{Bmatrix} \sigma_x \\ \sigma_y \\ \tau_{xy} \end{Bmatrix} = [T]^{-1}\begin{Bmatrix} \sigma_1 \\ \sigma_2 \\ \tau_{12} \end{Bmatrix}. \tag{3.4}$$

Now using Equation (3.4) it is possible to transform the stresses from one coordinate system to the other. Thus, the stresses in Equation (3.1) can be transformed from the principal material direction to the global directions. However, the strains are still in the principal material directions. To transform the strains from the principal material direction to the global directions we must first recognize that the strain measure

used here is engineering strain. Strickly speaking, engineering strains do not transform from one coordinate system to another; tensorial strains do. Thus, one must convert the engineering strains to tensorial strains, compute the transformation of the tensorial strain, the convert the tensorial strain back into engineering strain. The Reuter matrix:

$$[R]=\begin{bmatrix}1 & 0 & 0\\ 0 & 1 & 0\\ 0 & 0 & 2\end{bmatrix}, \tag{3.5}$$

can be used to convert engineering strain to tensorial strain by

$$\{e\}=[R]\{\varepsilon\} \qquad \text{or} \qquad \{\varepsilon\}=[R]^{-1}\{e\}. \tag{3.6}$$

Tensorial strain transformations from one coordinate system to the other by the same transformation matrix as the stresses. Therefore,

$$\{e_x\}=[T]\{e_1\}. \tag{3.7}$$

Therefore,

$$\{\varepsilon_x\}=[R]^{-1}\{e_x\} = [R]^{-1}[T]\{e_1\} = [R]^{-1}[T][R]\{\varepsilon_1\}$$

$$= [R]^{-1}[T][R]\{\varepsilon_1\}. \tag{3.8}$$

Then finally using Equations (3.1), (3.4) and (3.8), we find:

$$\{\sigma\}=[T]^{-1}[Q][R][T][R]^{-1}\{\varepsilon\}. \tag{3.9}$$

Using

$$[R][T][R]^{-1}=[T]^{-T}, \tag{3.10}$$

where the superscript T is matrix transpose. Equation (3.4) expands to

$$\begin{Bmatrix}\sigma_x\\ \sigma_y\\ \tau_{xy}\end{Bmatrix}=[T]^{-1}[Q][R][T][R]^{-1}\begin{Bmatrix}\varepsilon_x\\ \varepsilon_y\\ \gamma_{xy}\end{Bmatrix}. \tag{3.11}$$

To simplify Equation (3.11), let

$$\left[\bar{Q}\right] = [T]^{-1}[Q][T]^{-T}, \tag{3.12}$$

where $\left[\bar{Q}\right]$ is the transformed reduced stiffness matrix. The stress-strain relationship in the global, XY coordinates system becomes,

$$\begin{Bmatrix} \sigma_x \\ \sigma_y \\ \tau_{xy} \end{Bmatrix} = \begin{bmatrix} \bar{Q}_{11} & \bar{Q}_{12} & \bar{Q}_{16} \\ \bar{Q}_{12} & \bar{Q}_{22} & \bar{Q}_{26} \\ \bar{Q}_{16} & \bar{Q}_{26} & \bar{Q}_{66} \end{bmatrix} \begin{Bmatrix} \varepsilon_x \\ \varepsilon_y \\ \gamma_{xy} \end{Bmatrix}. \tag{3.13}$$

3.3 Laminate Mechanics

The macromechanical analysis defines the overall linear response of a multidirectional laminate subjected to in-plane forces and out-of-plane bending moments. The laminate properties are based on the macromechanical properties of the individual lamina. The laminate geometry is defined as if each ply were assembled on a flat surface, with the first ply, or lamina, on the bottom and the last ply on the top. The X-Y orientation is in-plane and the Z-axis is upward normal to the laminate and Z=0 is at the mid-thickness of the laminate.

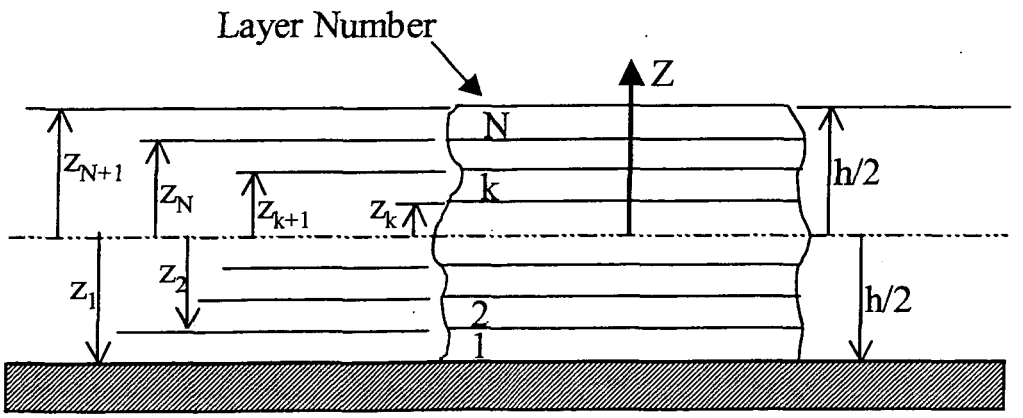

Figure 3.2. Nomenclature of an n-layered laminate.

A slight deviation in typical nomenclature is used to define the thickness of each ply; the initial index is 1 instead of the customary 0 as seen in most textbooks. Therefore, to define the ply thickness for each layer

$$t_i = z_{i+1} - z_i . \tag{3.14}$$

Equation (3.10) can be modified slightly to account for the stiffness of the lamina by adding a subscript k to represent each lamina within a laminate,

$$\begin{Bmatrix} \sigma_x \\ \sigma_y \\ \tau_{xy} \end{Bmatrix}_k = \begin{bmatrix} \overline{Q}_{11} & \overline{Q}_{12} & \overline{Q}_{16} \\ \overline{Q}_{12} & \overline{Q}_{22} & \overline{Q}_{26} \\ \overline{Q}_{16} & \overline{Q}_{26} & \overline{Q}_{66} \end{bmatrix}_k \begin{Bmatrix} \varepsilon_x \\ \varepsilon_y \\ \gamma_{xy} \end{Bmatrix}_k . \tag{3.15}$$

One of the basic assumptions of thin plate theory is that the strains are continuous through the thickness. This assumption is based on the continuity of displacements through the thickness, which is related to an assumption of perfect bonding between adjacent lamina. Based on the Kirchoff-Love displacement model, the components of strain consist of a stretching of the mid-plane and a linear variation of strain through the thickness of the laminate. Substituting the linear variation of strain into the transformed reduced stiffness stress-strain relationship results in

$$\begin{Bmatrix} \sigma_x \\ \sigma_y \\ \tau_{xy} \end{Bmatrix}_k = \begin{bmatrix} \overline{Q}_{11} & \overline{Q}_{12} & \overline{Q}_{16} \\ \overline{Q}_{12} & \overline{Q}_{22} & \overline{Q}_{26} \\ \overline{Q}_{16} & \overline{Q}_{26} & \overline{Q}_{66} \end{bmatrix}_k \left\{ \begin{Bmatrix} \varepsilon_x^0 \\ \varepsilon_y^0 \\ \gamma_{xy}^0 \end{Bmatrix} + z \begin{Bmatrix} \kappa_x \\ \kappa_y \\ \kappa_{xy} \end{Bmatrix} \right\}. \tag{3.16}$$

In classical lamination theory the focus is on the applied forces and moments acting on the laminate. Hence, the stresses are integrated through the thickness to determine the force and moment resultants. This yields

$$\begin{Bmatrix} N_x \\ N_y \\ N_{xy} \end{Bmatrix} = \int_{-\frac{h}{2}}^{\frac{h}{2}} \begin{Bmatrix} \sigma_x \\ \sigma_y \\ \tau_{xy} \end{Bmatrix} dz = \sum_{k=1}^{N} \int_{z_k}^{z_{k+1}} \begin{Bmatrix} \sigma_x \\ \sigma_y \\ \tau_{xy} \end{Bmatrix}_k dz \quad \text{and} \tag{3.17}$$

$$\begin{Bmatrix} M_x \\ M_y \\ M_{xy} \end{Bmatrix} = \int_{-\frac{h}{2}}^{\frac{h}{2}} \begin{Bmatrix} \sigma_x \\ \sigma_y \\ \tau_{xy} \end{Bmatrix} z dz = \sum_{k=1}^{N} \int_{z_k}^{z_{k+1}} \begin{Bmatrix} \sigma_x \\ \sigma_y \\ \tau_{xy} \end{Bmatrix}_k z dz \,. \tag{3.18}$$

Relating the force and bending resultants and the stress in terms of mid-plane strains and curvatures yield

$$\begin{Bmatrix} N_x \\ N_y \\ N_{xy} \end{Bmatrix} = \sum_{k=1}^{N} \begin{bmatrix} \overline{Q}_{11} & \overline{Q}_{12} & \overline{Q}_{16} \\ \overline{Q}_{12} & \overline{Q}_{22} & \overline{Q}_{26} \\ \overline{Q}_{16} & Q_{26} & \overline{Q}_{66} \end{bmatrix}_k \left\{ \int_{z_k}^{z_{k+1}} \begin{Bmatrix} \varepsilon_x^0 \\ \varepsilon_y^0 \\ \gamma_{xy}^0 \end{Bmatrix} dz + \int_{z_k}^{z_{k+1}} \begin{Bmatrix} \kappa_x \\ \kappa_y \\ \kappa_{xy} \end{Bmatrix} z dz \right\}, \tag{3.19}$$

$$\begin{Bmatrix} M_x \\ M_y \\ M_{xy} \end{Bmatrix} = \sum_{k=1}^{N} \begin{bmatrix} \overline{Q}_{11} & \overline{Q}_{12} & \overline{Q}_{16} \\ \overline{Q}_{12} & \overline{Q}_{22} & \overline{Q}_{26} \\ \overline{Q}_{16} & \overline{Q}_{26} & \overline{Q}_{66} \end{bmatrix}_k \left\{ \int_{z_k}^{z_{k+1}} \begin{Bmatrix} \varepsilon_x^0 \\ \varepsilon_y^0 \\ \gamma_{xy}^0 \end{Bmatrix} z dz + \int_{z_k}^{z_{k+1}} \begin{Bmatrix} \kappa_x \\ \kappa_y \\ \kappa_{xy} \end{Bmatrix} z^2 dz \right\}. \tag{3.20}$$

Noting that the mid-plane strains and curvatures are independent of z and the transformed reduced stiffness matrix is a constant within each lamina, the integrations can be replaced with summations

$$\begin{Bmatrix} N_x \\ N_y \\ N_{xy} \end{Bmatrix} = \begin{bmatrix} A_{11} & A_{12} & A_{16} \\ A_{12} & A_{22} & A_{26} \\ A_{16} & A_{26} & A_{66} \end{bmatrix} \begin{Bmatrix} \varepsilon_x^0 \\ \varepsilon_y^0 \\ \gamma_{xy}^0 \end{Bmatrix} + \begin{bmatrix} B_{11} & B_{12} & B_{16} \\ B_{12} & B_{22} & B_{26} \\ B_{16} & B_{26} & B_{66} \end{bmatrix} \begin{Bmatrix} \kappa_x \\ \kappa_y \\ \kappa_{xy} \end{Bmatrix} \quad \text{and} \tag{3.21}$$

$$\begin{Bmatrix} M_x \\ M_y \\ M_{xy} \end{Bmatrix} = \begin{bmatrix} B_{11} & B_{12} & B_{16} \\ B_{12} & B_{22} & B_{26} \\ B_{16} & B_{26} & B_{66} \end{bmatrix} \begin{Bmatrix} \varepsilon_x^0 \\ \varepsilon_y^0 \\ \gamma_{xy}^0 \end{Bmatrix} + \begin{bmatrix} D_{11} & D_{12} & D_{16} \\ D_{12} & D_{22} & D_{26} \\ D_{16} & D_{26} & D_{66} \end{bmatrix} \begin{Bmatrix} \kappa_x \\ \kappa_y \\ \kappa_{xy} \end{Bmatrix}. \tag{3.22}$$

where:

$$A_{ij} = \sum_{k=1}^{N} (\overline{Q}_{ij})_k (z_{k+1} - z_k), \tag{3.23}$$

is the extensional stiffness,

$$B_{ij} = \frac{1}{2} \sum_{k=1}^{N} \left(\overline{Q}_{ij}\right)_k \left(z_{k+1}{}^2 - z_k{}^2\right), \tag{3.24}$$

is the coupling stiffness (bending and extensional) and

$$D_{ij} = \frac{1}{3} \sum_{k=1}^{N} \left(\overline{Q}_{ij}\right)_k \left(z_{k+1}{}^3 - z_k{}^3\right), \tag{3.25}$$

is the bending stiffness.

3.4 Laminate Stiffness

The laminate under investigation in this research is an eight-ply quasi-isotropic laminate with a stacking sequence of $[0/+45/90/-45]_S$. The laminate is made from IM7/8552 graphite/epoxy unidirectional tape. The room temperature material properties for IM7/8552 are listed in Table 1. An individual cured ply thickness is assumed to be 0.0055 inches, resulting in a laminate 0.044 inches thick.

Table 3.1 IM7/8552 Graphite/Epoxy material properties

Property	Value
E_1	23.5 msi
E_2	1.2 msi
G_{12}	0.75 msi
ν	0.32

Utilizing CLT theory, stacking sequence, material property values, and ply thickness the stiffness matrices [A], [B], and [D] can be calculated. The in-plane extensional and shear stiffness matrix [A] is

$$[A]=\begin{bmatrix} 4.304x10^5 & 1.328x10^5 & 0 \\ 1.328x10^5 & 4.304x10^5 & 0 \\ 0 & 0 & 1.488x10^5 \end{bmatrix}\frac{lbf}{in}, \tag{3.26}$$

and the bending and torsional stiffness matrix [D] is

$$[D]=\begin{bmatrix} 113.7 & 14.4 & 11.2 \\ 14.4 & 39.1 & 11.2 \\ 11.2 & 11.2 & 17.0 \end{bmatrix} \quad \text{in*lbf.} \tag{3.27}$$

All terms within the extension-bending coupling matrix [B] are zero since the laminate is symmetric about the mid-plane, with respect to both geometry and material properties. Therefore, the in-plane and bending problems are decoupled. Thus, in-plane loads only produce in-plane strains and out-of-plane bending moments produce curvature. Hence

$$\begin{Bmatrix} N_x \\ N_y \\ N_{xy} \end{Bmatrix}=\begin{bmatrix} A_{11} & A_{12} & A_{13} \\ A_{12} & A_{22} & A_{26} \\ A_{16} & A_{26} & A_{66} \end{bmatrix}\begin{Bmatrix} \varepsilon_x^0 \\ \varepsilon_y^0 \\ \gamma_{xy}^0 \end{Bmatrix} \quad \text{and} \tag{3.28}$$

$$\begin{Bmatrix} M_x \\ M_y \\ M_{xy} \end{Bmatrix}=\begin{bmatrix} D_{11} & D_{12} & D_{16} \\ D_{12} & D_{22} & D_{26} \\ D_{16} & D_{26} & D_{66} \end{bmatrix}\begin{Bmatrix} \kappa_x \\ \kappa_y \\ \kappa_{xy} \end{Bmatrix}, \tag{3.29}$$

where the terms of [A] and [D] are defined above.

Chapter Four

Approach

4.1 Introduction

This chapter describes the structural analysis approach used for the CBPA and the additional studies performed to support the observations. The panel design and other relevant design features, such as taper angle, that are incorporated into a finite element analysis are described. Accuracy and confidence studies of the finite element model results were determined. Next, the analysis task to support the CBPA was performed. The study of the strain results indicate the objectives of the test have been met. Furthermore, a study of the out-of-plane displacements led to additional investigations of the bending stiffness matrix.

4.2 Panel Design Standardization

The composite panels used in the permeability testing were constructed from different material systems, but were standardized to a specific laminate thickness and ply orientation. This design standardization simplified the analysis; allowing one analysis to be valid for all composite materials to be tested. The assumption being that all materials tested will have similar stiffness and strength characteristics. Sparks lists the materials tested; the variation among the panels is the matrix type, and in some cases, the curing process employed. All panels used IM7 carbon fiber. Thus, this assumption seems appropriate. Sparks describes the design standardization as 25-inch diameter panels, *eight plies thick*, and are constructed using the quasi-isotropic stacking sequence of

$[0/45/-45/90]_S$. The thicknesses ranged from 0.035 to 0.045 inches. The analysis to support this thesis assumed each cured ply to be 0.0055 inches, resulting in a panel thickness of 0.044 inches. There is a difference in the diameter of the test panel and that of the finite element model. However, the inner diameter of the Invar rings did not change, thus the additional panel width was constrained between the two Invar rings and does not invalidate the analysis. This was a last minute change to incorporate an increase in bolt diameter.

4.3 Finite Element Model

The finite element model is described in Chapter 5. Initially, a quarter-symmetry model employing symmetric boundary conditions was employed for the analysis. However, inaccuracies in the assumption of symmetry required a model for the entire plate. Studies were performed to determine a method to apply the complex boundary conditions to the model to simulate the assembly and testing of the panels. For example, the panel is free to slip inward during assembly but is fully constrained during pressurization. Therefore, a geometric nonlinear NASTRAN analysis was used, not only for the large displacements expected by the panel, but also to allow the end conditions from the assembly to become the initial conditions for the pressurization and facilitate a change in boundary restraint. A mesh convergence study among four models with globally increasing mesh density was performed to ensure the mesh density was sufficient to provide reasonable results. Convergence procedures for finite element models are not well defined. The ideas from Spyrakos [10] are employed, such as comparing stresses among models and comparing finite element solutions to theoretical

solutions. Many theoretical solutions for a variety of circular plate configurations are available. However, none have the specific boundary conditions of the CBPA. The linear elastic, isotropic finite element studies solving circular plates of known solutions provide confidence in the modeling technique.

4.4 Analysis

The objectives of the analysis task were to support the development of the CBPA by providing the required pressure to achieve a desired strain level and determine the diameter of an equal biaxial strain area. The initial assessment quickly indicated that the strains near the boundary required mitigation. Options such as adding and tapering plies near the edge were considered, as well as increasing the diameter of the apparatus. These options proved unfeasible, due to the increasing complexity of manufacturing and the deviation from the goal of a simple test. Pre-stressing the panel by introducing a forced rotation at the boundary proved to be a viable solution. However, the magnitude of the forced rotation needed to be determined. The forced rotation, also referred to as the taper angle, produced bending in the panel such that the outer fiber was in tension and inner fiber in compression. Pressurization would tend to reverse the bending, thus reduce the fiber strains. By incrementally increasing the taper angle and applying a consistent pressure among the iterations sufficient to develop the desired strain level, the optimum taper angle was determined. Once determined, this angle was used throughout the remainder of the analysis and for the convergence studies.

The pressure required to achieve the 4000 microstrain level in the center of the panel was determined by averaging the inner and outer fiber strains of an element near

the center of the panel. The strains versus pressure are presented in Chapter 5. It should be noted however, that the pressure applied in an actual test was based on the strain measurement; therefore, inaccuracies of the strain readings in such a severe environment are possible and panel integrity must be assured for the potentially higher pressures. A pressure of 60 psi was required, and the analysis indicated that a typical panel could withstand a pressure of 100 psi.

Uniaxial tests only fully strain in one direction; transverse strains are much smaller. The lack of significant transverse strain will likely not develop microcracking within certain unidirectional plies; therefore, a network of cracks will not form and allow gas to permeate through the entire thickness. An equal biaxial strain ratio ensures each ply is fully strained in two directions, thus microcracks are more likely to occur in all plies and a network of cracks may form and allow gas to permeate through the entire thickness. The intent of determining the diameter of an equal biaxial area was to facilitate the permeability measurement procedure, with a collecting device to capture the hydrogen permeation through a known area. However, Sparks [9] describes the challenges encountered with this measurement approach and described another method. Nevertheless, the analytical determination of the equal biaxial area provided insight into the mechanics of the plate.

Recall the design of the testing apparatus used a stainless steel bucket to form a cryogenic volume with the panel. The combination of two Invar rings and composite plate was bolted to the flanges of the bucket. The bolt holes in the stainless steel flanges were oversized to allow relative motion between the Invar/composite system and the stainless steel flanges. The analysis indicated that the increase of load in the panel due to

the free thermal contraction of the Invar/composite system was negligible. Therefore, the analysis ignored the effects of the liquid hydrogen.

4.5 Bending Stiffness Matrix, [D]

A study of the bending stiffness matrix was initially performed by simply repeatedly altering the orientation of the plies by positive five-degrees and tabulating the resulting six terms of the bending stiffness at each increment. After realizing the bending stiffness for a balanced and symmetric laminate varies depending on ply orientation relative to a rotating structural axes, a more in-depth investigation into the theoretical equations was performed. The result was a MathCAD program, used to calculate the stiffness matrices of a laminate, enabling a study of the stiffness terms as a function of angular position. The MathCAD program, presented in Appendix A, calculates the extensional, coupling and bending stiffness matrices as a function of position around the periphery. It also plots each stiffness term on a polar plot, similarly to Tsai [11]. The laminate plate equations from Bower are investigated and simplifications are imposed based on the properties of the laminate. The equations provide insight into understanding the behavior of the plate due to the flexural boundary conditions.

4.6 I-Beam Analogy

It was recognized that the bending stiffness terms as a function of angular position, in particular D_{11} and D_{22}, can be visualized by treating the laminate as an I-beam. The elementary mechanics of materials approach for calculating the moment of inertia about an axis for an I-beam, using the Parallel Axis Theorem, can also be used to

calculate the laminate bending stiffness D_{11} and D_{22}. Each ply is treated as a flange, offset from the neutral axis (mid-plane) by its corresponding position in the laminate. Therefore, the cross section appears as a web-less beam with four pairs of symmetric flanges of different widths. The flange width represents the $\overline{Q}_{ij}$ value of each ply relative to the structural axes.

Chapter 5

RESULTS

5.1 Introduction

This chapter presents the analytical results and observations from the investigation of the CBPA. Most of the results were developed using a finite element model. A description of the finite element model is presented followed by a convergence study for the model. Also presented are the finite element model confidence study results of a circular plate of known solutions. Following the confidence study is the analysis results of the CBPA that includes the taper angle optimization study and the determination of the equal biaxial strain field in the composite panel. The last section is based on observations of the analysis results that led to an in-depth study of the composite laminate bending stiffness matrix.

5.2 Finite Element Model

NASTRAN finite element models using four-node quadrilateral, CQUAD4, plate elements and two-node CBEAM beam elements were built for the investigation. In the development of the model, the symmetry of the geometry and loading initially suggests that a shorter "run-time" for the analysis is available through modeling a segment of the plate, such as a half or quarter of the plate. Obviously, an isotropic circular plate with a pressure load is axially symmetric and the symmetry of the problem can be used to reduce the computational time necessary to analyze the response. However, a rectilinearly orthotropic circular plate does not possess axisymmetry. This is shown in

Section 5.6. Consequently, the model used for this analysis is a full 360° model of the plate, without assumption of symmetry.

The boundary conditions imposed on the model simulate the clamped region at the edge. The boundary conditions enforce the nodal displacements and rotations of the clamped region to match a twelve-degree taper angle. A cylindrical coordinate system located in the middle of the panel is referenced by all nodes except the center node. To prevent the model from rotating about an axis normal to the plate, an outer node is constrained from tangential displacement. To prevent in-plane rigid body translation, the center node is constrained in x and y directions and references the global rectangular coordinate system. Pressure is applied to the model via NASTRAN PLOAD4 cards. Each node with a radial coordinate less than 10.5 inches is referenced by the PLOAD4 cards and each node with a radial coordinate equal to or greater than 10.5 inches is subject to the forced displacement and rotation.

A ring of NASTRAN CBEAM elements are located at a radius of 10.5 inches and have a large cross sectional area and moment of inertia. The function of the CBEAMs is to impose the proper boundary constraints for the two-step NASTRAN nonlinear analysis. The CBEAMS allow the panel to freely contract radially during assembly and restrict the panel from radial movement during pressurization. This is accomplished by initially assigning the CBEAM elements a warm temperature on the order of 800 degrees F. Subsequently, during the iterations of the nonlinear assembly case, the CBEAMs are cooled to room temperature and constrict radially the same amount as the panel, resulting in no additional load due to the presence of the CBEAMS. Then, during the nonlinear pressurization steps, the stiff CBEAMs do not respond to the pressure, thus

the panel is restrained from moving radially. This process was checked by comparing the assembly stresses between models with and without CBEAMs, demonstrating a negligible change in stress.

IM7-977-2 is one of the materials used during the testing [9]. However, at the initiation of the CBPA investigation, room temperature material properties for IM7-8552 were readily available. It is assumed that the material properties between the two systems are similar since both use the same fibers and similar resin. The material properties for IM7-8552 are shown in Table 3.1 in Section 3.4. The material properties, E_{11}, E_{22}, G_{12}, and ν_{12}, which reference the material coordinate system for the lamina, are the inputs for a two-dimensional orthotropic material. A composite laminate is created by stacking eight layers of the lamina with ply orientations of 0,+45,90,-45,-45,90,+45,0 with respect to the structural x-y axes. A NASTRAN MAT8 card is used to define the 2-D orthotropic properties of the plies and a NASTRAN PCOMP card defines the stacking sequence the composite laminate.

5.3 Convergence Study

Recall the objectives of the CBPA analysis are to determine the required pressure to achieve a desired strain level in the middle of the panel and to ensure panel integrity. A convergence study was performed to gain confidence in the finite element model to ensure satisfactory results. The four finite element models used in the convergence study are shown in Figure 5.1.

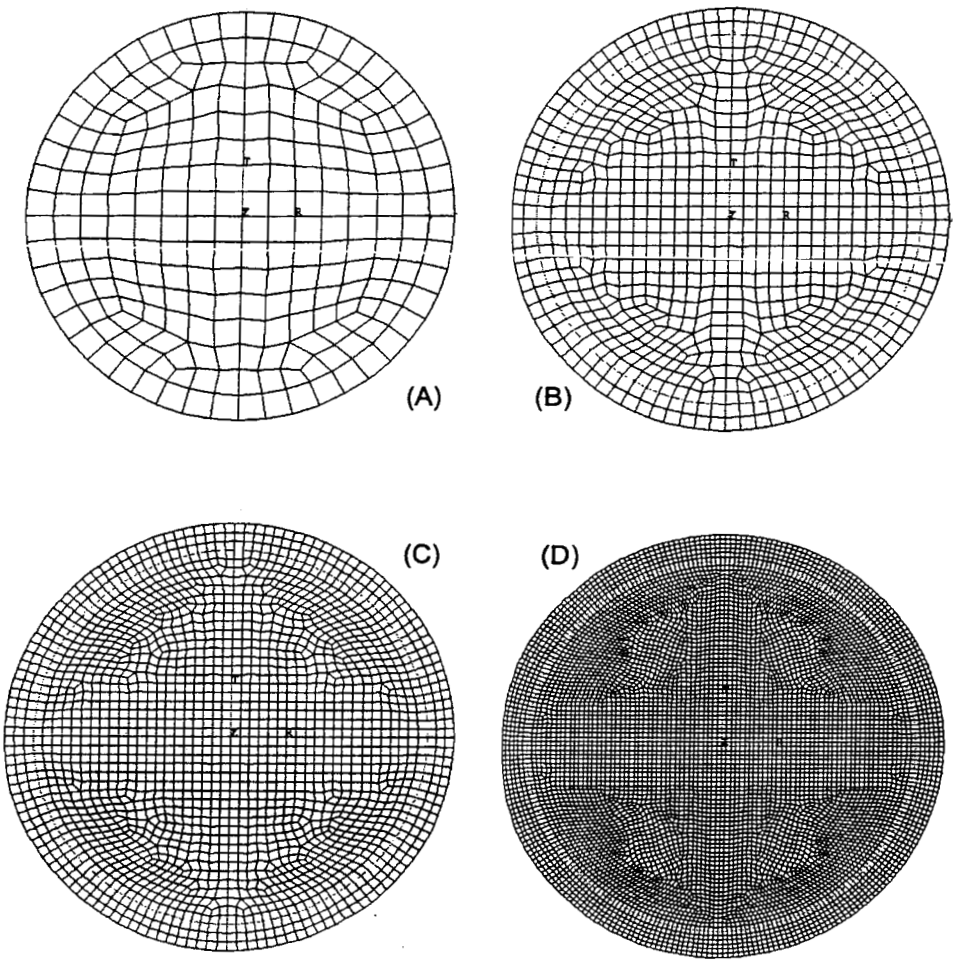

Figure 5.1 Finite element models used in convergence study.

The four models are referred to as (A) 1.5 inch, (B) 0.75 inch, (C) 0.5 inch, and (D) 0.25 inch models. The size reference is based on a typical element size in the model. Thus, in the 1.5 inch model, a typical element is approximately 1.5 inch by 1.5 inch. Table 5.1 shows the key model characteristics among the four models. The typical element size for each model and the corresponding degrees of freedom (DOF) are shown. The number of nodes and elements of each model are presented. As shown in Table 5.1, as the typical element size decreases, the degrees of freedom increase.

Table 5.1 Comparison of the finite element models.

Model	Nominal Dimension	DOF	Nodes	CQUAD4	CBEAMS
A	1.50	1590	265	240	48
B	0.75	5382	897	852	88
C	0.50	12174	2029	1960	136
D	0.25	45822	7637	7504	264

Each new model with more degrees of freedom, thus higher mesh density, is an attempt to refine the model, with the intention to improve the result. The first convergence study was based on the outer fiber stress at the center of the panel. The assembly condition is investigated as well as the assembly plus pressure. The percent difference between successive mesh refinements is calculated using the following equation,

$$\text{Percent Difference} = \left|\frac{\text{MODEL}_1 - \text{MODEL}_2}{\text{MODEL}_2}\right| * 100 . \qquad (5.1)$$

In Equation 5.1, 'model 2' represents the finite element model with the most refinement. This form of the equation assumes that 'model 2' calculates an answer more accurately than the preceding finite element model, 'model 1'.

Table 5.2. FEM percent difference for outer fiber stress.

Assembly		
Model	Stress (psi)	% Diff
A	4,716	-
B	5,401	12.68
C	5,641	4.25
D	5,786	2.51

Assembly + 60 psi		
Model	Stress (psi)	% Diff
A	100,120	-
B	101,587	1.44
C	101,853	0.26
D	102,589	0.72

The percent differences of outer fiber stresses at the center of the panel show that the percent difference decreases for the assembly case with increasing mesh density and the combination of assembly and pressure indicate all models produce acceptable results.

McKinney [7] presents another method to study the convergence of finite models of increasing mesh refinement. He uses a convergence criterion of $\Delta\sigma/\Delta DOF < 0.10$ between successive model results. Below, in Table 5-3, $\Delta\sigma/\Delta DOF$ results for the assembly and assembly plus pressure are presented. For both load cases, the convergence criterion between models A and B is not met; thus model A is not converged. The convergence criterion between models B and C is less than the convergence criterion, thus model B has converged based on $\Delta\sigma/\Delta DOF = 0.04$ for both load cases.

Table 5.3 Convergence study results.

Assembly						
Model	DOF	Stress (psi)		ΔDOF	Δσ	Δσ/ΔDOF
A	1590	4716				
B	5382	5401	B-A	3792	685	0.18
C	12174	5641	C-B	6792	240	0.04
D	45822	5786	D-C	33648	145	0.00
Assembly + 60 psi						
Model	DOF	Stress (psi)		ΔDOF	Δσ	Δσ/ΔDOF
A	1590	100120				
B	5382	101587	B-A	3792	1467	0.39
C	12174	101853	C-B	6792	266	0.04
D	45822	102589	D-C	33648	736	0.02

Another model result of the panel used to study the convergence was the maximum fiber strain of the panel near the boundary. The severe bending due to assembly created localized strain discontinuities as shown in Figure 5.2. This discontinuity is fictitious and

the result of the model. It is the result of the discontinuity in the boundary condition. Note in the plot that the strains calculated at the periphery of the panel are increasing with decreasing mesh size, which is evidence that the discontinuity is a result of the model. However, this localized peak was reduced once the pressure was added. (See Section 5.5 Analysis of the Test Apparatus) The mesh convergence studies indicated additional mesh refinement was required near the boundary; however, additional edge refinement would provide a negligible increase in confidence in panel integrity.

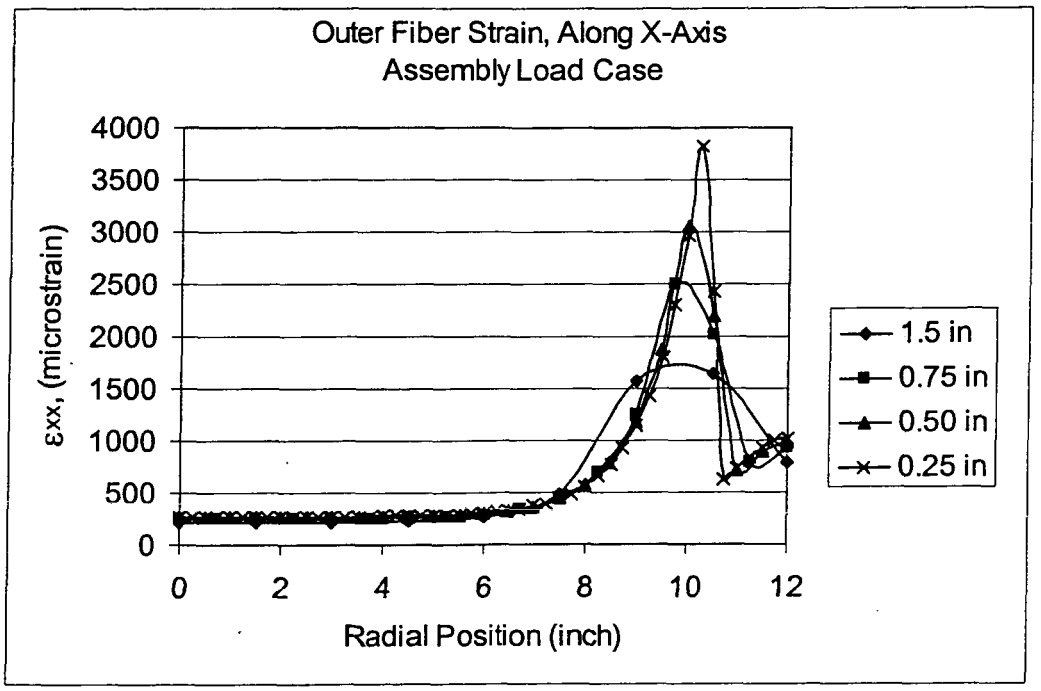

Figure 5.2 Outer fiber ε_{xx} strains along x-axis.

5.4 Confidence Study

Another investigation to support the validity of the finite element model utilized comparisons to known solutions. Four circular, flat plate solutions from Cook [4] were used as study cases. Figure 5.3 provides a graphical representation of the four cases.

Each case provided a linear response of an isotropic circular plate of constant thickness with a uniform pressure or a centrally concentrated load. The boundary conditions used for the studies were either fixed or simply supported. Finite element results of normal displacements and edge moments were compared to the analytical solution.

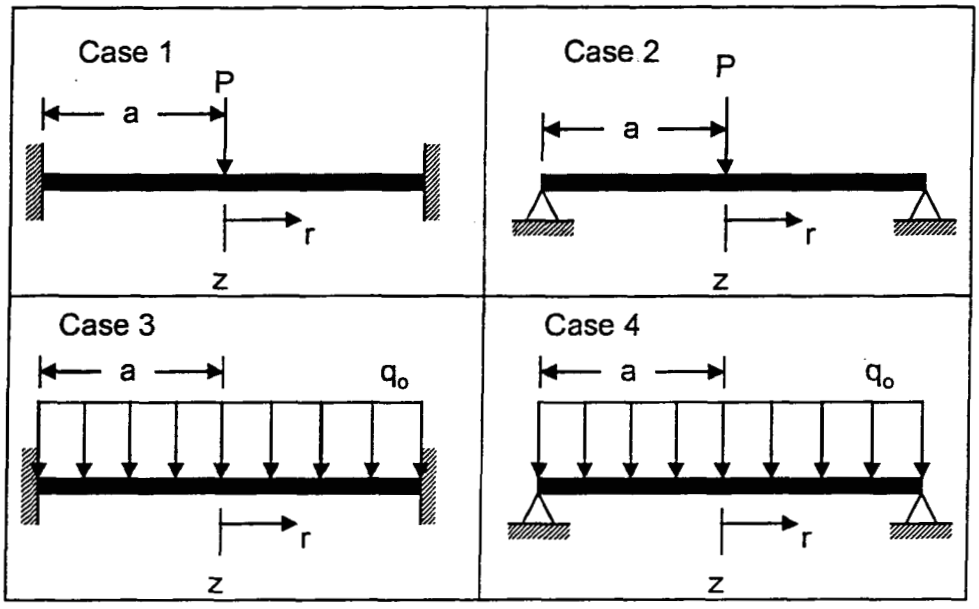

Figure 5.3 Four circular plate problems used in confidence study.

For all cases, a is the radius of the plate and is defined as 10.5 inches. The isotropic plate bending stiffness D is in terms of constants E, Young's Modulus, t, plate thickness and Poisson's ratio, n = 0.3. For this study, the Young's Modulus is $10 * 10^6$ psi and the thickness is 0.10 inches. The bending stiffness can be determined by

$$D = \frac{Et^3}{12(1-\nu^2)}, \tag{5.2}$$

and is used in the calculation of normal displacement, w in the positive z direction. Expressions for displacements and bending moments are functions of radial position, r. P

is the concentrated load of 10 lbf in the center of the plate and qo is the distributed load of 2 psi.. Note, for Cases 1 through 4 below, all equations are from Cook [4].

Case 1 has a fixed boundary condition and a concentrated load of P in the middle of the plate. The normal displacement w as a function of radial position r is

$$w(r) = \frac{P}{16\pi D}\left(2r^2 \ln\frac{r}{a} + a^2 - r^2\right), \tag{5.3}$$

and the maximum deflection is

$$w_{max} = \frac{Pa^2}{16\pi D} \text{ at } r = 0. \tag{5.4}$$

The radial moment Mr, or the bending moment due to radial stresses, is determined by

$$M_r(r) = -\frac{P}{4\pi}\left[1 + (1+\nu)\ln\frac{r}{a}\right] \text{ and} \tag{5.5}$$

$$M_r = 0.0796P \text{ at the boundary.} \tag{5.6}$$

Case 2 has a simple support boundary condition and a concentrated load P in the middle. The normal displacement w as a function of radial position r is

$$w(r) = \frac{P}{16\pi D}\left(\frac{3+\nu}{1+\nu}\left(a^2 - r^2\right) + 2r^2 \ln\frac{r}{a}\right), \tag{5.7}$$

and the maximum deflection is

$$w_{max} = 0.0505\frac{Pa^2}{D} \text{ at } r = 0. \tag{5.8}$$

The radial moment Mr is zero at a simple support boundary.

Case 3 has a fixed boundary condition and a distributed load qo over the entire plate. The normal displacement w as a function of radial position r is

$$w(r) = \frac{q_o}{64D}\left(a^2 - r^2\right)^2, \tag{5.9}$$

and the maximum deflection is

$$w_{max} = \frac{q_o a^4}{64D} \text{ at } r = 0. \tag{5.10}$$

The radial moment Mr is determined by

$$M_r(r) = -\frac{q_o}{16}\left[(1+\nu)a^2 - (3+\nu)r^2\right] \text{ and} \tag{5.11}$$

$$M_r = 0.125 q_o a^2 \text{ at the boundary.} \tag{5.12}$$

Case 4 has a simple support boundary condition and a distributed load qo over the entire plate. The normal displacement w as a function of radial position r is

$$w(r) = \frac{q_o\left(a^2 - r^2\right)}{64D}\left(\frac{5+\nu}{1+\nu}a^2 - r^2\right), \tag{5.13}$$

and the maximum deflection is

$$w_{max} = 0.0637\frac{q_o a^4}{D} \text{ at } r = 0. \tag{5.14}$$

The radial moment Mr is determined by

$$M_r(r) = -\frac{q_o}{16}\left[(1+\nu)a^2 - (3+\nu)r^2\right] \text{ and} \tag{5.15}$$

Mr is zero at a simple support boundary.

Table 5.4 summarizes the comparison of the finite element results and the theoretical solutions. The percent error in the displacements and edge moments for the four case studies is calculated using

$$\text{Percent Error} = \frac{|\text{measured} - \text{actual}|}{\text{actual}} * 100 \tag{5.16}$$

Table 5.4 Displacement and edge moment comparisons between theory and FEM.

Normal Displacement	FEM	Cook[x]	Percent Error
Case 1	0.024	0.024	1.7
Case 2	0.060	0.061	1.3
Case 3	0.417	0.415	0.5
Case 4	1.690	1.691	0.1

Edge Moment	FEM	Cook[x]	Percent Error
Case 1	0.754	0.796	5.2
Case 2	N/A	N/A	N/A
Case 3	24.400	27.562	11.5
Case 4	N/A	N/A	N/A

The finite element analysis and the theoretical solutions agree within a 2% error for the normal displacement at the center of the panel. The percent error for the edge moment at the boundary is approximately 12% for case 3. However, the finite element result for the radial moment as a function of radius agrees with the theoretical calculation for all values of r except for the edge. The 12% error does not cause concern, since the edge is known to produce erratic results as shown previously in Section 5.3.

5.5 Analysis of Test Apparatus

5.5.1 Taper Angle Optimization

The initial investigation of the pressure required to achieve the desired strain level had a flat, fixed boundary (clamped edge) that produced extremely large strains near the boundary. To relieve the strain level, the clamped boundary had an angle introduced, which is defined for this research as the taper angle. The taper angle was accomplished in the design by machining opposing angles on the corresponding mating surfaces producing a wedge-like shape for each Invar ring, as shown in Figure 1.2. When assembled, the two rings force the composite plate to conform to the taper, enforcing a uniform rotation and displacement of the outer 1.5 inches. The subsequent pressure load will reverse the bending direction, relieving the assembly strains.

The finite element model was utilized to determine the optimum taper angle by minimizing the boundary strains for the combination of assembly and pressure load. Taper angles for the assembly case were increased in one-degree increments and the maximum assembly stresses were noted. The procedure utilized the nonlinear solution capability of NASTRAN, allowing the end condition of the assembly case to be the initial condition of the pressure case. Figure 5.4 a graph of the maximum stresses within the plate as a function of the taper angle for the assembly and pressure load conditions. This graph shows that the assembly stresses increase with increasing taper angle due to increased bending. Also, the graph indicates a downward trend in the assembly plus pressure cases. This is due to the pressure relieving the assembly strains. Figure 5.4 shows that the minimum stresses for the assembly plus pressure condition occurs for a taper angle of approximately twelve degrees.

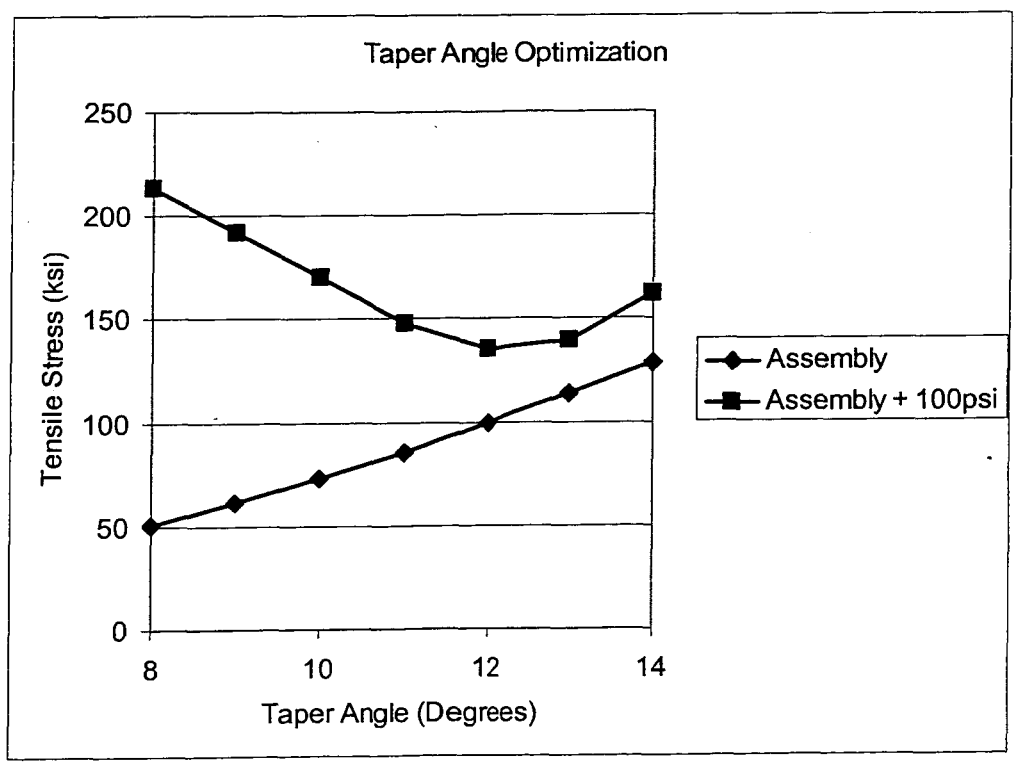

Figure 5.4. Optimization of the taper angle to minimize stresses in composite panel.

The taper angle optimization is a function of lamina stiffness, laminate stacking sequence, and total thickness. This is important from a design standpoint because deviations from the standard panel configuration as described in Section 4.2 would invalidate the taper angle optimization and increases the risk of panel failure from either the assembly or pressure case.

5.5.2 Equal Biaxial Strain Region

The objectives of the test required 4000 microstrain at the center of the panel. The nonlinear finite element solution indicates that a pressure of approximately 60 psi will produce the desired strain level. In Figure 5.5, the inner and outer surface strains of an element near the center of the panel are shown for the entire loading sequence of assembly and pressure. During the assembly case, the strains are tensile which indicates the membrane behavior of the panel is greater than the bending. The two strain curves due to pressure show a nonlinear response, with the strains increasing rapidly during the initial pressure loading and the rate decreasing at higher pressures. The relative difference between the inner and outer strains indicates that bending is present in the panel, but is small compared to the in-plane tensile strains. The pressure creates both a membrane response and a bending response as indicated by the inner and outer strain levels in the center of the panel.

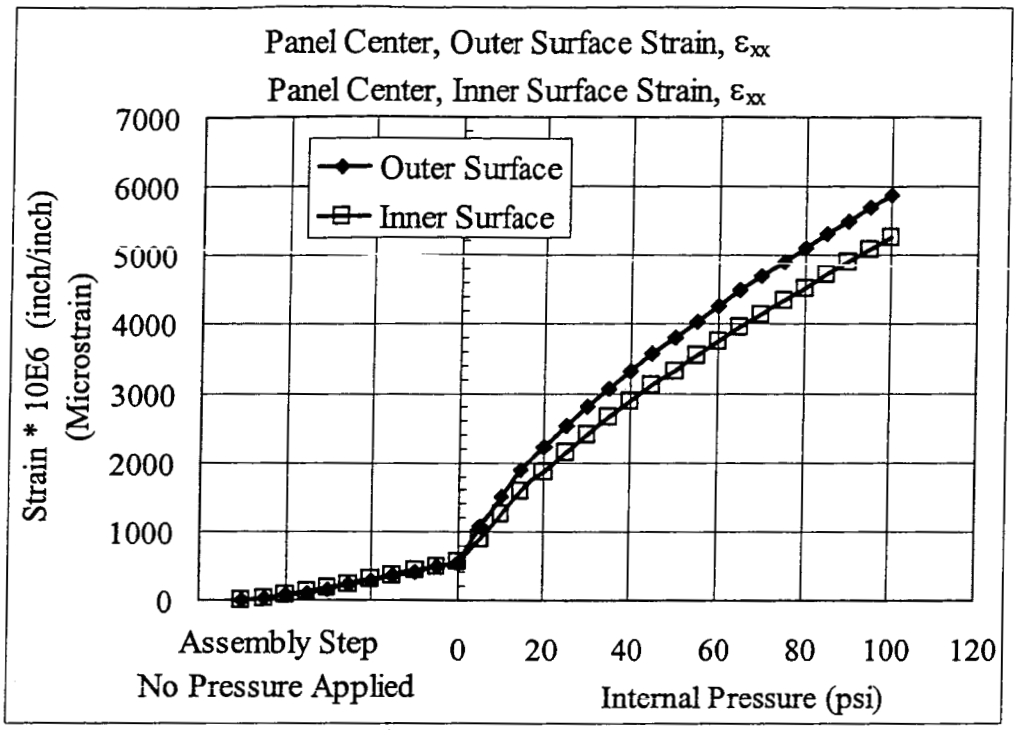

Figure 5.5. Outer fiber strain at the center of panel.

The permeability testing was limited to an area containing an equal biaxial strain ratio. Strain ratios other than equal biaxial were excluded from the permeability measurement region because it was desirable to have all eight plies strained to the same level in two directions, thus if the strain level was sufficient to cause microcracking, than the microcracking would likely be present in all the plies. Then, a network of crack may develop throughout the thickness and allow hydrogen to permeate.

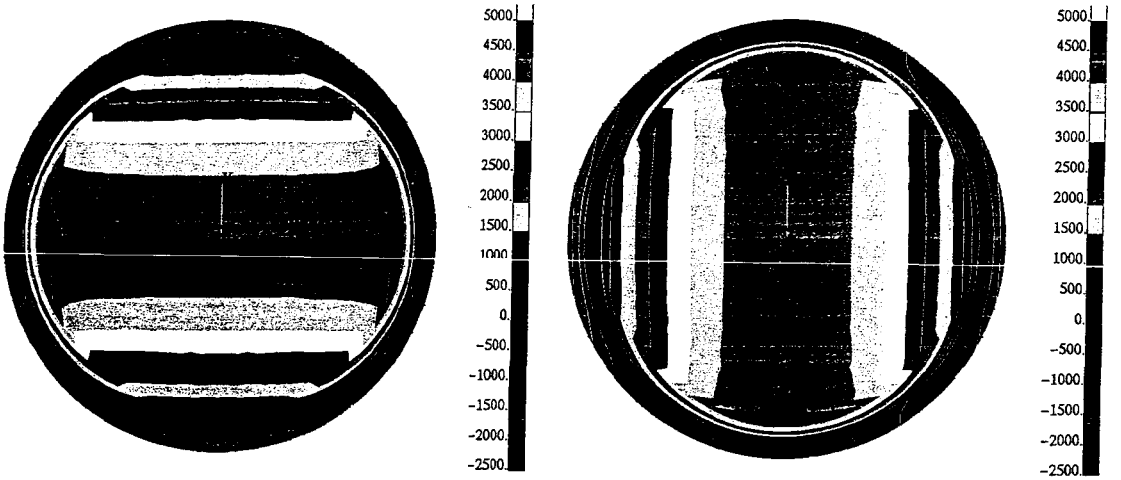

Outside Layer, ε_{xx} Outside Layer, ε_{yy}

Figure 5.6. Outer fiber strains in the material coordinate system.

Recall Figure 5.5, which indicates a pressure of 60 psi should produce ε_{xx} between 4000 and 4500 microstrain. Figure 5.6, a fringe plot, which displays several ranges of data, each range a specific color, is shown. The fringe plot shows the outside longitudinal and transverse strains, ε_{xx} and ε_{yy} respectively, in the principal material directions. The ε_{yy} strain behaves similarly to ε_{xx}, but is rotated ninety degrees. Figure 5.7 graphs the two strain components along the structural x-axes. For ε_{xx}, the strain level remains fairly uniform along the principal material direction. However, in the transverse material direction, ε_{yy} drops off quickly away from the center. A ratio between 1:1 and 1.05:1 was considered equal-biaxial, which established about 4.5 inches as the desired diameter. Figure 5.8 graphs the strain ratio between ε_{xx} and ε_{yy}. It was also concluded that the strain ratio was independent of angle. Also, as the area of interest moves radially outward from the center, the equal biaxial ratio strain ratio begins to deteriorate, reducing to a 2:1 ratio at an eight inch radius. It should be noted that the original permeability measurement apparatus used a two inch diameter area for permeability measurements [9].

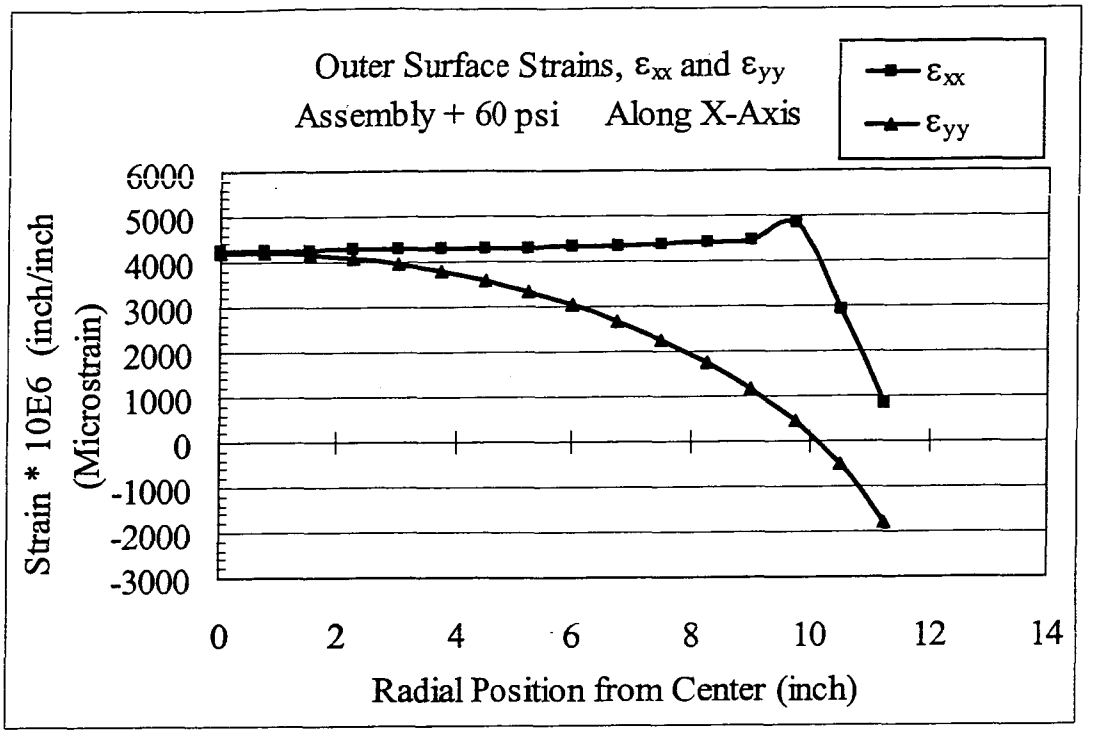

Figure 5-7. Outer fiber strains along the structural x-axis.

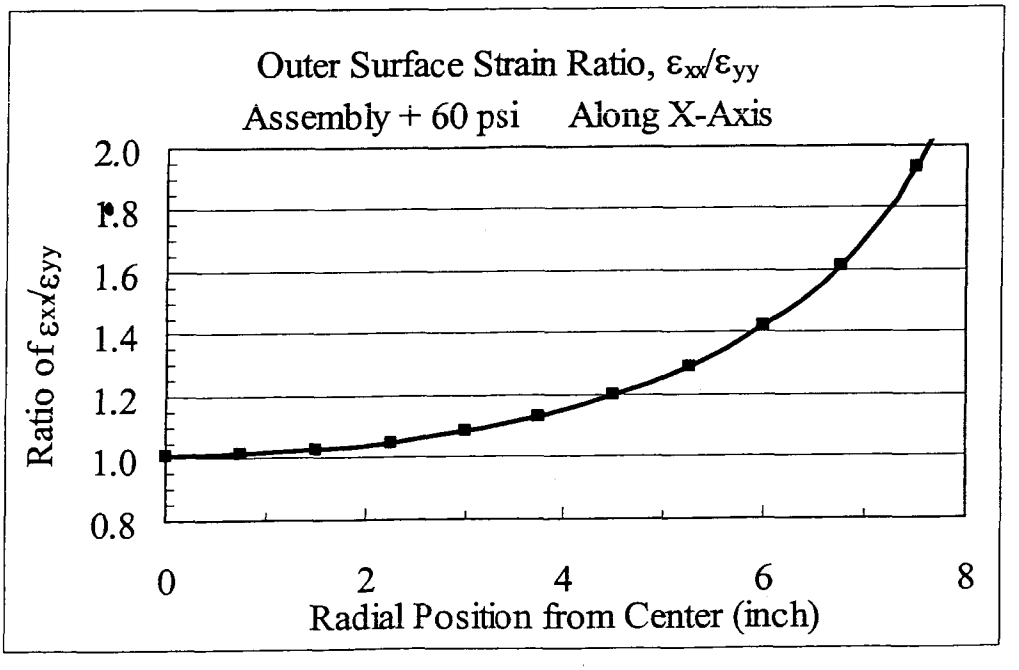

Figure 5-8. Outer fiber biaxial strain ratio.

5.6 Displacement

For the assembly, a flat composite panel is forced to rotate about a concentric line 10.5 inches from the center, as shown earlier in Figure 1.2. The outer annular area from the 10.5 inch radius to the 12 inch outside diameter is forced to conform to the twelve-degree angle of the Invar rings. Once assembled, the panel maintains this deformation state during the pressurization. The pressure results in bulging of the panel, reversing the assembly stresses. Figure 5.9 graphs the out-of-plane displacements of the panel due to assembly and pressure along the structural x-axes. The resulting dome profile indicates that the problem was indeed a geometric nonlinear solution based on δz, out-of-plane displacement, being greater than 10 times the plate thickness.

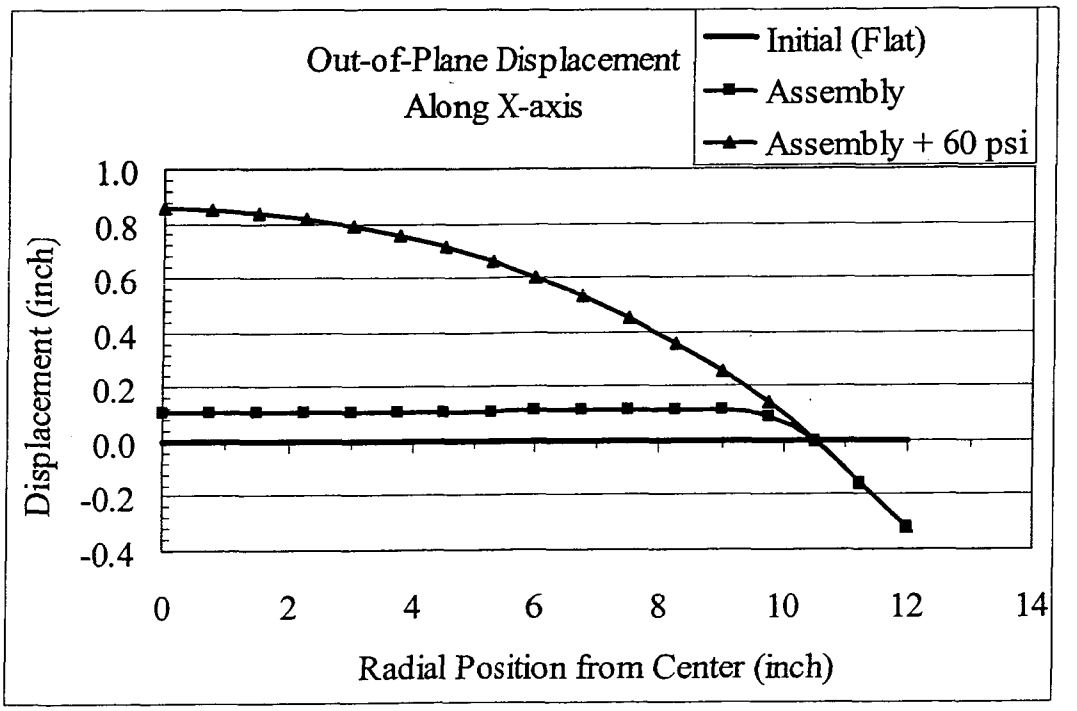

Figure 5.9. Out-of-plane displacement of the panel.

A closer inspection of the out-of-plane assembly displacements calculated by the finite element model reveals an unexpected and intriguing pattern. The expected result

for the normal displacements of an isotropic plate is that the displacements at a particular radius are the same around the plate, i.e., the response is axisymmetric and independent of angle around the plate. The results in Figures 5.10 and Figure 5.11 show the out-of-plane displacement for the assembly case. Of particular interest in these figures is that there is no evidence of axisymmetry in the results. In both plots, constant values of the normal displacement occur on the periphery of a rounded square, which is skewed from the structural x- and y-axes. Figure 5.10 is a fringe plot of the out-of-plane displacements, from a range of 0.10 inches to 0.185 inches. Therefore, the displacements due to the taper, which have values of negative z, are not included. The displacement pattern shown in Figure 5.10 indicates that the normal displacements are not aligned with the principal directions. Furthermore, the maximum out-of-plane displacement is not even in the center of the panel. The skewed nature of the displacements relative to the principal directions is the unexpected result alluded to previously.

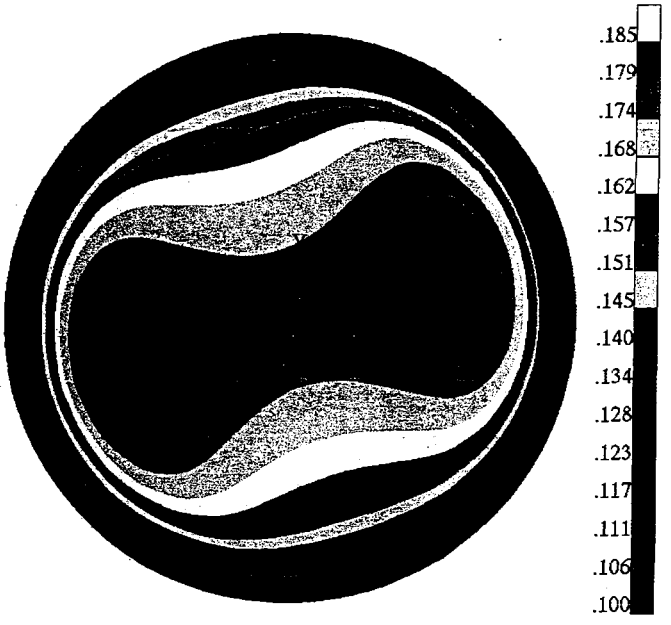

Figure 5.10 Plot of normal displacements.

Figure 5.11 is a graph of the out-of plane displacements along the x- and y- structural axes from the center to the edge. Note the annular clamped region is identified. Along the x-axis, observing from center to edge, the out-of-plane displacements initially are flat, then tend to slightly rise between approximately four to eight inches in radius. On the contrary, the out-of-plane displacements along the y-axes continuously decrease with increasing radius.

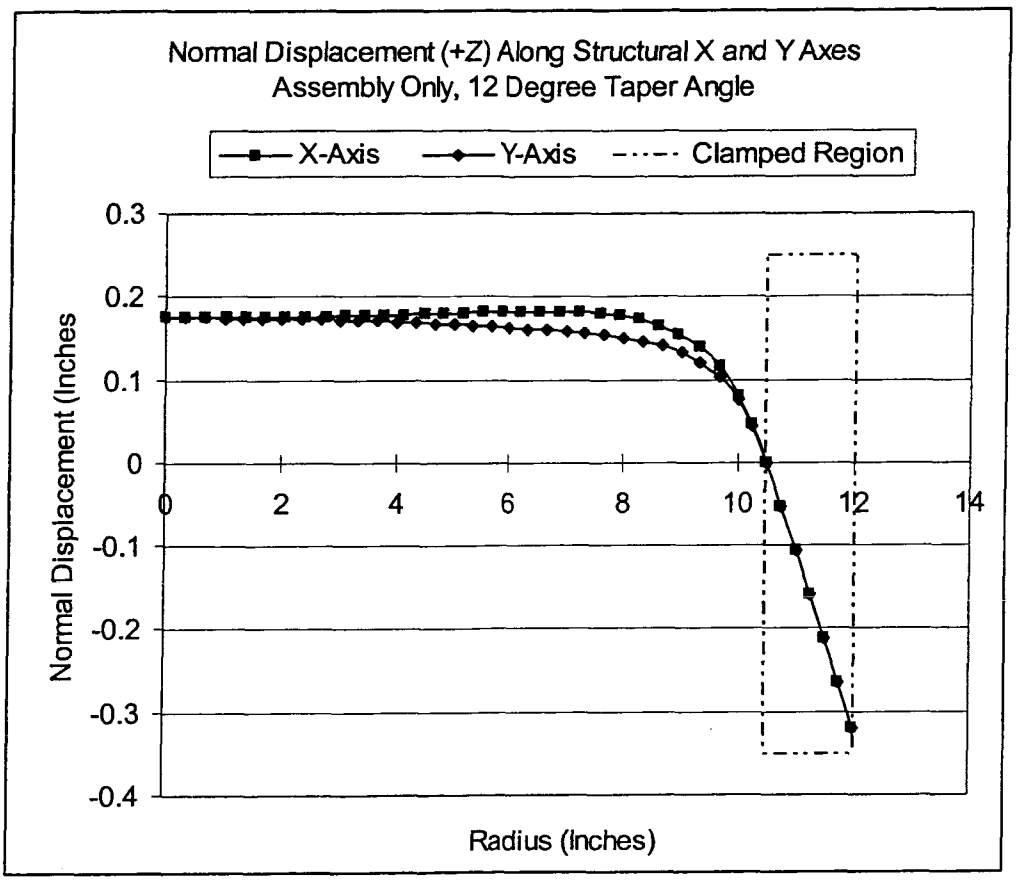

Figure 5.11. The normal displacements along the structural axes due to assembly and taper angle of twelve degrees.

The unusual displacement results lead to a study to determine how such a displacement pattern can be generated by a balanced, symmetric, quasi-isotropic composite circular plate subjected to a uniform, twelve-degree rotation at the boundary.

5.7 Bending Stiffness Matrix [D] Study

For the plate under investigation in this research, the stiffness terms of the in-plane matrix [A] are independent of the azimuth angle, θ, and constant throughout the plate. The stacking sequence is balanced, symmetric, and quasi-isotropic. Consequently, all the terms of the coupling stiffness [B] are zero. Therefore, any non-symmetrical behavior of the response is due to either the loading condition or the bending stiffness [D]. The assembly loading condition and the pressure loading condition are both axisymmetric. Therefore, an initial assessment predicts that the non-symmetric behavior in the response is due purely to the bending stiffness.

To illustrate that the non-symmetrical behavior is due to the bending stiffness, the bending stiffness in a cylindrical coordinate system is calculated. A MathCAD program, shown in Appendix A, calculates the bending stiffness for an angle of interest. The program still assumes a rectangular coordinate system, but the coordinate system is rotated by $+\alpha$. Therefore, the original lamina orientations will be modified by $-\alpha$. Thus, the 0-degree ply will now have an orientation of $-\alpha$. Assume the angle of interest, α is +15-degrees, the lamina orientations relative to the new coordinate system will be $[-15/30/75/-75]_S$. A different bending stiffness matrix [D] based on the new x'-y' coordinate system is determined. By repeating the process for the entire circumference of the plate, calculating and tabulating the six terms of [D] at each angle α, the variation of the bending stiffness matrix in a cylindrical coordinate system can be determined. Figure 5.12 on the following page contains a graphical representation of the six terms of the bending stiffness matrix as a function of angular position around the circumference. Recall the bending stiffness matrix [D] relative to the principal direction is,

$$[D] = \begin{bmatrix} 113.7 & 14.4 & 11.2 \\ 14.4 & 39.1 & 11.2 \\ 11.2 & 11.2 & 17.0 \end{bmatrix} \text{in} * \text{lb}. \tag{5.17}$$

The D_{11} and D_{22} values are 113.7 and 39.1 respectively, and these two values are identified on the graph in Figure 5.12. It is observed that only D_{12} and D_{66} are symmetric with respect to the principal direction. D_{11} and D_{22} are both asymmetric with respect to the principal axes. However, D_{11} and D_{22} are out-of-phase by 90-degrees and are equivalent at α = - 30 and +60 degrees. However, the relative maximum and minimum values of D_{11} and D_{22} are not off-set by 90-degrees. The maximum value and corresponding angle of interest for D_{11} are approximately 117 in*lb and +10 degrees, respectively. The minimum value and corresponding angle of interest for D_{22} is approximately 27in*lb and +25 degrees respectively. The MathCAD program can determine the local minimums and maximums by taking the derivative of the bending term of interest. Also shown is the Euclidian norm of the matrix [D], calculated using

$$Eu = \left[\sum_{i=1}^{3} \sum_{j=1}^{3} \left[(D_{ij})^2 \right] \right]^{\frac{1}{2}}, \tag{5.18}$$

as a relative measure of the contribution of all the bending stiffness terms.

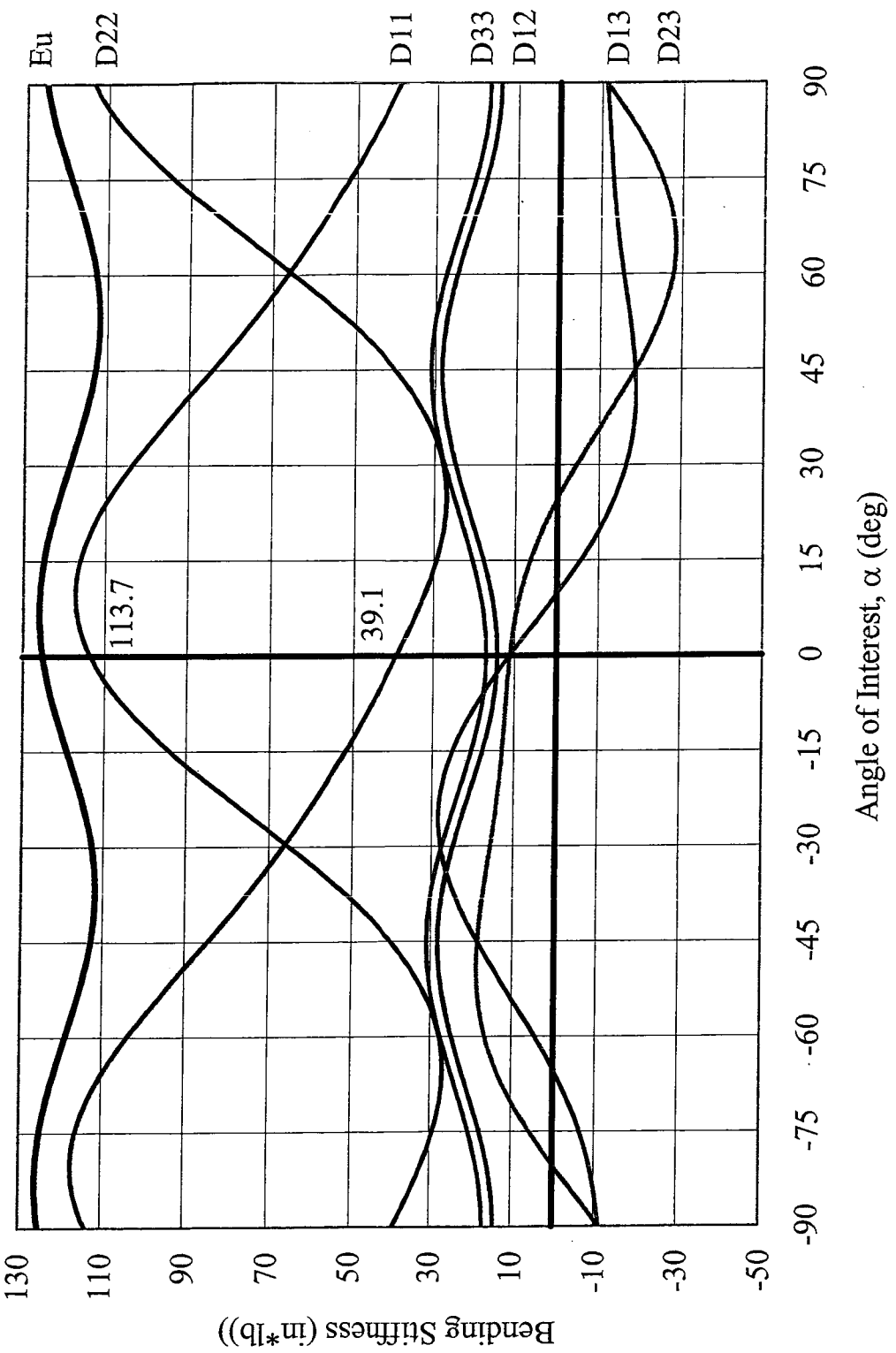

Figure 5-12. The stiffness terms of [D] in cylindrical coordinates.

Bailey [1] in her dissertation provides equations for the terms of the bending stiffness in terms of invariants. The six bending stiffness equations and the sixteen invariant equations found in Bailey are shown in Appendix B. The six bending stiffness terms are calculated and compared to the results from the previous approach. The two approaches agree in the calculation of the stiffness terms along the diagonal, D_{11}, D_{22} and D_{66}, but the off-diagonal terms do not agree. The D_{12} curves differ slightly; D_{16} and D_{26} appear to have a sign error. Since Bailey derived the equations, involving lengthy trigonometric identities, one of the equations may have a small error.

It is apparent that the variation of [D] is a contributor to the out-of-plane displacement results. Bower [2] derives the in-plane force balance equations for a laminate. To summarize his methodology, start with the force resultant equation for a laminate, Equation (3.21), and rewrite the equation in terms of $\frac{\partial N_x}{\partial x}$. Substitute for the strains and curvatures in terms of in-plane displacements and out-of-plane displacements. Repeat for $\frac{\partial N_{xy}}{\partial y}$ and substitute $\frac{\partial N_x}{\partial x}$ and $\frac{\partial N_{xy}}{\partial y}$ into the plate equations for equilibrium of an infinitesimal plate element for the x-direction, results in the following from Bower,

$$A_{11}\frac{\partial^2 u}{\partial x^2}+2A_{16}\frac{\partial^2 u}{\partial x\partial y}+A_{66}\frac{\partial^2 u}{\partial y^2}+A_{16}\frac{\partial^2 v}{\partial x^2}+(A_{12}+A_{66})\frac{\partial^2 v}{\partial x\partial y}+A_{26}\frac{\partial^2 v}{\partial y^2}$$
$$+B_{11}\frac{\partial^2 w}{\partial x^3}+3B_{11}\frac{\partial^3 w}{\partial x^2\partial y}+(B_{12}+2B_{66})\frac{\partial^3 w}{\partial x\partial y^2}+B_{21}\frac{\partial^2 w}{\partial y^3}=0 \qquad (5.19)$$

Using the same procedure, the equations for N_y and N_{xy} of Equation 3.21 we find

$$A_{16}\frac{\partial^2 u}{\partial x^2}+(A_{12}+A_{66})\frac{\partial^2 u}{\partial x\partial y}+A_{26}\frac{\partial^2 u}{\partial y^2}+A_{66}\frac{\partial^2 v}{\partial x^2}+2A_{26}\frac{\partial^2 v}{\partial x\partial y}+A_{22}\frac{\partial^2 v}{\partial y^2}$$
$$+B_{16}\frac{\partial^2 w}{\partial x^3}+(B_{12}+B_{66})\frac{\partial^3 w}{\partial x^2\partial y}+3B_{26}\frac{\partial^3 w}{\partial x\partial y^2}+B_{22}\frac{\partial^2 w}{\partial y^3}=0 \qquad (5.20)$$

It has been observed that for this laminate, the in-plane stiffness terms $[A_{ij}]$ are independent of α and the bending-coupling terms $[B_{ij}]$ are zero for all angles. Thus, Equations (5.19) and (5.20) can be reduced to

$$A_{11}\frac{\partial^2 u}{\partial x^2}+2A_{16}\frac{\partial^2 u}{\partial x\partial y}+A_{66}\frac{\partial^2 u}{\partial y^2}+A_{16}\frac{\partial^2 v}{\partial x^2}+(A_{12}+A_{66})\frac{\partial^2 v}{\partial x\partial y}+A_{26}\frac{\partial^2 v}{\partial y^2}=0 \quad (5.21)$$

and

$$A_{13}\frac{\partial^2 u}{\partial x^2}+(A_{12}+A_{33})\frac{\partial^2 u}{\partial x\partial y}+A_{23}\frac{\partial^2 u}{\partial y^2}+A_{33}\frac{\partial^2 v}{\partial x^2}+2A_{23}\frac{\partial^2 v}{\partial x\partial y}+A_{22}\frac{\partial^2 v}{\partial y^2}=0 \quad (5.22)$$

An inspection of the two equations indicates that the in-plane displacements, u and v, are not affected by α and, as Bower points out, that if B_{ij} are zero, then the out-of-plane displacement, w, is decoupled. Therefore, the in-plane loads do not produce out-of-plane displacements. However, investigating the out-of-plane plate equations from Bower indicates the presence of in-plane loads and their contribution to the out-of-plane displacement. The full out-of-plane displacement equation from Bower, ignoring dynamic effects is

$$\begin{aligned}&D_{11}\frac{\partial^4 w}{\partial x^4}+4D_{16}\frac{\partial^4 w}{\partial x^3\partial y}+(2D_{12}+4D_{66})\frac{\partial^4 w}{\partial x^2\partial y^2}+4D_{26}\frac{\partial^4 w}{\partial x\partial y^3}+D_{22}\frac{\partial^4 w}{\partial y^4}\\&+\overline{N}_x\frac{\partial^2 w}{\partial x^2}+2\overline{N}_{xy}\frac{\partial^2 w}{\partial x\partial y}+\overline{N}_y\frac{\partial^2 w}{\partial y^2}=-p(x,y)\end{aligned} \quad (5.23)$$

Note that this equation has in-plane forces that contribute to the out-of-plane displacement, and are present, in this case, due to the boundary conditions.

5.8 I-Beam Analogy

In Chapter 3, the bending stiffness matrix [D] was written as

$$D_{ij} = \frac{1}{3}\sum_{k=1}^{N}\left(\overline{Q_{ij}}\right)_k\left(z_k{}^3 - z_{k-1}{}^3\right), \tag{5.24}$$

where Q_{ij} is the material constants for a ply and z defines the position of a ply relative to the mid-plane. Bower [2] presents an alternative expression for the bending stiffness in terms of the centroid, z-bar, and thickness, t, of the plies,

$$D_{ij} = \sum_{k=1}^{N}\overline{Q}_{ij_k}\left(t_k\bar{z}_k{}^3 + \frac{1}{12}t_k{}^3\right). \tag{5.25}$$

Bower presents an analogous relationship between bending stiffness for an isotropic plate, D, and the bending stiffness of a beam, EI. Through the use of the Parallel Axis Theorem, he concludes the "laminate stiffness is the summation of the bending stiffnesses of the individual lamina about the mid-plane" [2]. In this thesis, this analogy is presented graphically for the circular plate, to visualize the contribution of each ply to the total bending stiffness of the laminate and the variation of the bending stiffness as a function of angular position.

Visualization of the analogy between the bending stiffness of a laminated plate and an I-beam is accomplished using the D_{11} bending stiffness term as an illustration. Solving for D_{11} requires computing the transformed reduced stiffness for each ply, Q_{11k}. Jones [6] provides an equation,

$$\overline{Q}_{11} = Q_{11}\cos^4\theta + 2(Q_{12} + 2Q_{66})\sin^2\theta\cos^2\theta + Q_{22}\sin^4\theta, \tag{5-19}$$

to calculate the transformed reduce stiffness of each ply based on the a ply's orientation with respect to a structural axes. The Q_{ij}'s can be determined by Equation 3-2. The $\overline{Q}_{11}$ for the two 0-degree plies is 23.6 msi, 7.15 msi for the four 45-degree plies, and 1.21 for

the two 90-degree plies. For graphical purposes, normalizing each $\overline{Q}_{11}$ with respect to the principal material direction, and graphing ply index versus normalization value yields a profile similar to an I-beam cross section, as shown below in Figure 5.13.

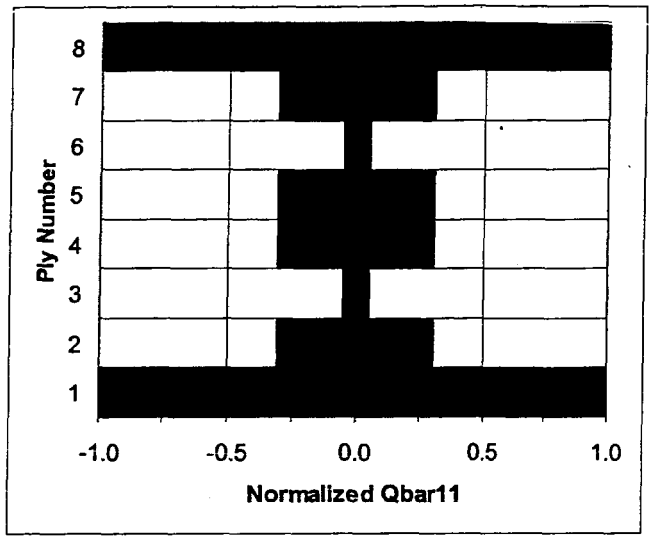

Figure 5.13. Normalization of $\overline{Q}_{11}$ for each ply at 0-degrees, along x-axis.

In Figure 5.13, ply 1 and ply 8 represent the two 0-degree plies, which normalize to 1.0. The four 45-degree plies, 2, 4, 5 and 7, normalize to 0.3 and the two 90-degree plies normalize to 0.05. The $\overline{Q}_{11}$ for each ply represents the moment of inertia of a rectangular beam about its' centroid [2] and are the $\frac{\overline{Q}_{11}t_k^{\,3}}{12}$ from Equation (5.25). Using the Parallel Axis Theorem, the $A*d^2$ term corresponds to $\overline{Q}_{11k}t_k\bar{z}_k^{\,2}$ of Equation (5.25). In Table 5.5, the $\overline{Q}_{11}$ and normalized $\overline{Q}_{11}$ are presented for each ply as well as the contribution each ply has to the total D_{11} value.

Table 5.5 Contribution of each ply to the overall stiffness value.

Ply	Qbar11	Normalized	D
1	23.6	1.00	48.47
2	7.2	0.30	7.53
3	1.2	0.05	0.47
4	7.2	0.30	0.40
5	7.2	0.30	0.40
6	1.2	0.05	0.47
7	7.2	0.30	7.53
8	23.6	1.00	48.47
		Summation->	113.75

Rotating the structural axes x-y ninety degrees to a new x'-y'axes, the orientations of the plies relative to x'-y' change by minus ninety degrees. The stacking sequence becomes $[-90/-45/0/45]_S$ in the x'-y' coordinate system. Figure 5.14 illustrates I-beam analogy for the location 90 degrees from the x-y axes.

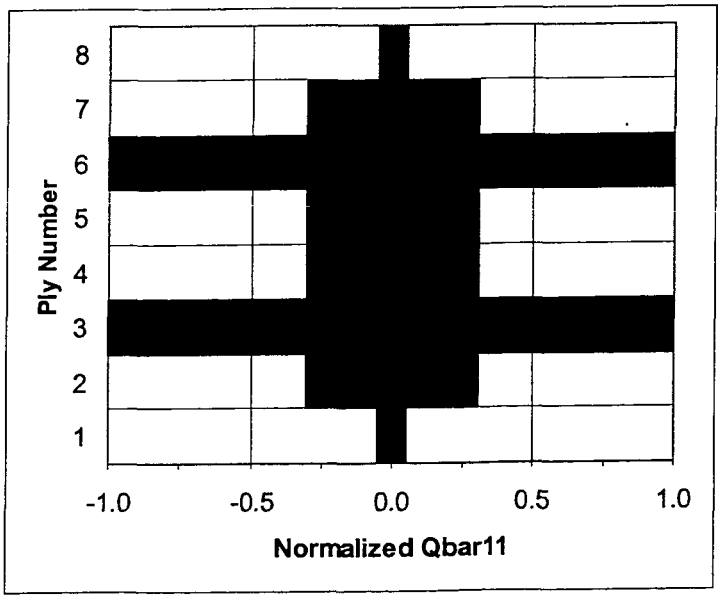

Figure 5.14. Normalization of $\overline{Q}_{11}$ for each ply at 90-degrees, along y-axis.

In the I-beam analogy plot of Figure 5.14, the two outer plies contribute very little to the overall laminate bending stiffness. Plies 3 and 6 contribute the most to the total stiffness,

followed closely by plies 2 and 7, because their distance from the mid-plane and the usage of the Parallel Axis Theorem increase their contribution.

In Table 5.6, the corresponding $\overline{Q}_{11}$ and normalized $\overline{Q}_{11}$ are presented for each ply based on a rotation of 90 degrees. The contribution of each ply to the total D_{11} is listed.

Table 5.6 Contribution of each ply to the overall stiffness value.

Ply	Qbar11	Normalized	D
1	1.2	0.05	2.48
2	7.2	0.30	7.53
3	23.6	1.00	9.17
4	7.2	0.30	0.40
5	7.2	0.30	0.40
6	23.6	1.00	9.17
7	7.2	0.30	7.53
8	1.2	0.05	2.48
		Summation->	39.15

Another angle of interest for the D_{11} terms as a function of angle is where $D_{11}=D_{22}$, at an angle of interest of ~60 degrees. Figure 5.15 shows the D_{11} on the left and D_{22} on the right. Both cross sections have different characteristics. The D_{22} has a fairly stiff representation for the outer plies, where as D_{22}'s outer ply is not as stiff. The contribution of the outer ply for D_{22} is approximately the same contribution as plies 6 and 7 for D_{11}, as shown in Table 5.7.

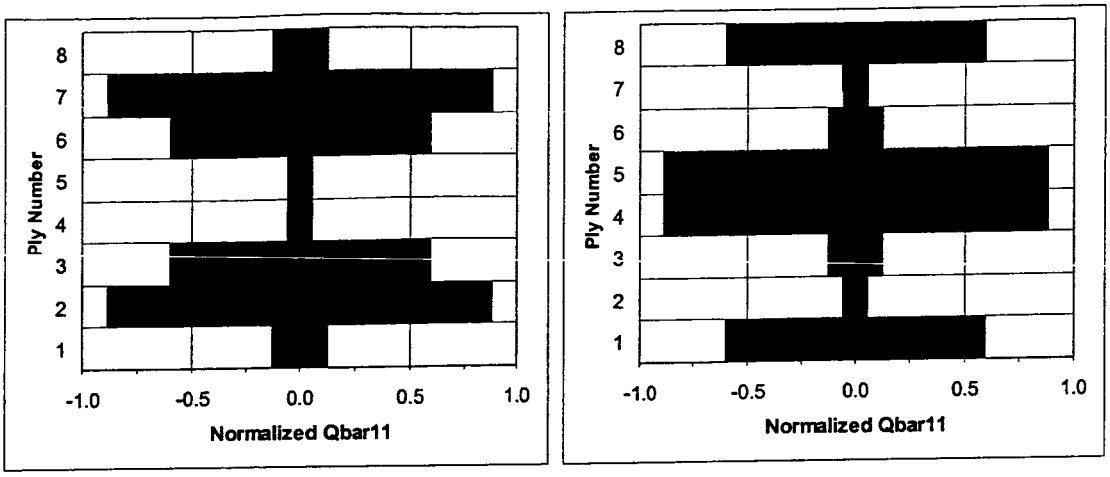

Figure 5.15 D_{11} and D_{22} at 60 degrees.

Table 5.7 Comparison between D11 and D22 at angle 60 degrees.

Ply	Qbar11	Normalized	D
1	2.9	0.12	5.87
2	20.8	0.88	21.92
3	14.1	0.60	5.46
4	1.4	0.06	0.08
5	1.4	0.06	0.08
6	14.1	0.60	5.46
7	20.8	0.88	21.92
8	2.9	0.12	5.87
		Summation->	66.67

Ply	Qbar11	Normalized	D
1	14.1	0.60	28.87
2	1.4	0.06	1.47
3	2.9	0.12	1.11
4	20.8	0.88	1.15
5	20.8	0.88	1.15
6	2.9	0.12	1.11
7	1.4	0.06	1.47
8	14.1	0.60	28.87
		Summation->	65.21

Chapter 6

CONCLUSIONS

The thesis was based on a structural analysis to support a specialized materials test, the cryogenic biaxial permeability apparatus (CBPA). Sparks [9] points out that the CBPA test program was successful. The test demonstrated the advertised capability to screen material systems for propensity to microcrack and permeate after repeated cycles of cryogenic exposure and mechanical strain. Thus, the original tasks of providing the required pressure to achieve a desired strain level and ensure panel integrity were successfully demonstrated based on the success of the test program. In fact, none of the twenty-five test panels failed catastrophically. They failed due to excessive permeation and inability to sustain pressure.

There is not a general procedure to follow to determine finite element model convergence. The two methods used in this thesis follow the same trend of increasing mesh density increases the accuracy of the results. However, the increasing mesh density was applied globally, instead of locally. It is obvious from the stresses due to pressure that each model sufficiently calculates the stresses in the middle of the panel. Therefore, the middle of the panel did not need any mesh refinement. However, the outer fiber strains near the boundary indicate that more mesh refinement is required. Therefore, convergence studies and mesh refinement are likely to be unique for a particular finite element model. Each requires a more thorough evaluation, taking into account stress gradients, areas of interest, areas previously converged, etc.

The unusual displacement result of the panel that was subjected to edge bending was shown to be from the flexural plate equations. The investigation showed the

buckling terms as a result of flexure, can produce the out-of-plane response seen in the finite model results.

The variation in the bending stiffness terms as a function of angular position has been shown to lack the expected orthogonal nature with respect to a convenient structural axis. A symmetric, balanced, laminate coupled with the assumption of symmetric boundary conditions could lead to inaccurate results.

The I-Beam analogy is a good illustrative tool for visualizing the contribution of each ply. It has applications not only for the bending stiffness, as shown in this work, but also for the [A] and [B] stiffness terms.

REFERENCES

[1] Bailey, Michelle, 1998. "Polar Plate Theory for Orthogonal Anisotropy," University of Alabama in Huntsville Dissertation.

[2] Bower, Mark W., 2000. *Composite Materials*, The University of Alabama in Huntsville.

[3] Cavallaro, P., Gee, L., and Tsangarakis, N., 1995. "Biaxial Testing of Composites – A Study of the Disk Specimen," *ARL-TR-690*

[4] Cook, R. D., 1985. *Advanced Mechanics of Materials*, Macmillan Publishing Company.

[5] Grimsley, B. W., Cano, R. J., Johnson, N. J., Loos, A. F., McMahon, W. M., 2001. "Hybrid Composites for LH2 Fuel Tank Structure."

[6] Jones, R. M., 1975. *Mechanics of Composite Materials*, Hemisphere Publishing Corp.

[7] McKenney, David R., 1995. "A Comparison of the H and P Versions of the Finite Element Method in a Practical Engineering Application," University of Alabama in Huntsville Thesis.

[8] MIL-HDBK-17A

[9] Sparks, J, S., 2003. "Development of a Cryobiaxial Permeability Apparatus to Measure Hydrogen Permeability in Composites." *NASA/TM-2003-212928.*

[10] Spyrakos, Constantine C. 1994. *Finite Element Modeling in Engineering Practice*, West Virginia University Press.

[11] Tsai, Stephen W., 1992. Theory of Composite Design, Think Composites.

[12] Goetz, R., Ryan, R. and Whitaker, A.F., 2000. "Failure Report of the X-33 Liquid Hydrogen Tank Test Investigation Team." NASA Marshall Space Flight Center, Huntsville, AL

Composite Laminate Properties
Stan Oliver, MSFC
October 2004

This MathCAD worksheet calculates the [A], [B], and [D] stiffness matrices of a composite laminate. The required inputs are the longitudinal and transverse modulus of elasticity of the lamina as well as the shear modulus of elasticity and the Poisson's ratio. Laminate design parameters, such as thickness and orientation of each ply are input as an array, with the index of the array corresponding to the ply indentification number.

The inputs for the lamina properties can be changed to an array input to facilatate usage of different materials

New Units:

$msi := 1000 \cdot 1000 \cdot psi$

$lb := lbf$

MODULUS OF ELASTICITY OF LAMINA

IM7/977-2 Room Temperature Properties

$E_{11} := 23.5 \cdot 10^6 \cdot psi$ $\quad \upsilon_{12} := 0.32$

$E_{22} := 1.2 \cdot 10^6 \cdot psi$ $\quad G_{12} := \frac{E_{11}}{2 \cdot (1 + \upsilon_{12})}$ $\quad G_{12} = 8.902 \times 10^6\ psi$

$\upsilon_{21} := \frac{E_{22}}{E_{11}} \cdot \upsilon_{12}$ $\quad G_{12} := 7.5 \cdot 10^5 \cdot psi$

LAMINATE STACKING SEQUENCE

$$\theta := \begin{pmatrix} 0 \\ 45 \\ 90 \\ -45 \\ -45 \\ 90 \\ 45 \\ 0 \end{pmatrix} \cdot deg$$

NUMBER OF LAYERS, N

$N := rows(\theta)$

$N = 8$

$k := 1 .. N$

LAMINA THICKNESSES

$$t := \begin{pmatrix} .0055 \\ .0055 \\ .0055 \\ .0055 \\ .0055 \\ .0055 \\ .0055 \\ .0055 \end{pmatrix} \cdot in \qquad t_{tot} := \sum_k t_k$$

$$t_{tot} = 0.044\,in$$

LAMINATE STIFFNESS VALUES

Since all layers are same material, each layer material property can be defined as:

$E1_k := E_{11}$ $\qquad$ $\upsilon 12_k := \upsilon_{12}$

$E2_k := E_{22}$ $\qquad$ $\upsilon 21_k := \upsilon_{21}$

$G12_k := G_{12}$ $\qquad$ $\upsilon 21_k := E2_k \cdot \frac{\upsilon 12_k}{E1_k}$

$\theta^T = (0 \;\; 45 \;\; 90 \;\; -45 \;\; -45 \;\; 90 \;\; 45 \;\; 0)\,deg$

$E_{11} = 2.35 \times 10^7\,psi$

$E_{22} = 1.2 \times 10^6\,psi$

DEFINITION OF LAMINIATE

Laminate height (thickness) $\qquad h := t_{tot} \qquad h = 0.044\,in$

Mid-plane $\qquad z_1 := \frac{-h}{2} \qquad z_1 = -0.022\,in$

Ply location for each layer $\qquad z_{k+1} := z_k + t_k$

$z_1 = -0.022\,in$

$z_2 = -0.017\,in$

$z_3 = -0.011\,in$

$z_4 = -5.5 \times 10^{-3}\,in$

$z_5 = 0\,in$

$z_6 = 5.5 \times 10^{-3}\,in$

$z_7 = 0.011\,in$

$z_8 = 0.017\,in$

$z_9 = 0.022\,in$

REDUCED STIFFNESS MATRIX OF LAMINA, [Q]

$$Q(k) := \begin{pmatrix} \frac{E1_k}{1 - \upsilon 12_k \cdot \upsilon 21_k} & \upsilon 21_k \cdot \frac{E1_k}{1 - \upsilon 12_k \cdot \upsilon 21_k} & 0 \\ \upsilon 12_k \cdot \frac{E2_k}{1 - \upsilon 12_k \cdot \upsilon 21_k} & \frac{E2_k}{1 - \upsilon 12_k \cdot \upsilon 21_k} & 0 \\ 0 & 0 & G12_k \end{pmatrix}$$

$$Q(1) = \begin{pmatrix} 2.362 \times 10^7 & 3.86 \times 10^5 & 0 \\ 3.86 \times 10^5 & 1.206 \times 10^6 & 0 \\ 0 & 0 & 7.5 \times 10^5 \end{pmatrix} psi$$

Now, the ABD matrices will be recalculated as a function of angular position from the global X axis. The angle alpha α is the angle of interest and the ABD matrices will be relative to the axis parallel to alpha.

$\alpha := -180 \cdot deg, -175 \cdot deg .. 180 \cdot deg$ Range of alpha from -180 degrees to + 180 degrees

$$T(k, \alpha) := \begin{pmatrix} \cos(\theta_k - \alpha)^2 & \sin(\theta_k - \alpha)^2 & 2 \cdot \cos(\theta_k - \alpha) \cdot \sin(\theta_k - \alpha) \\ \sin(\theta_k - \alpha)^2 & \cos(\theta_k - \alpha)^2 & -2 \cdot \cos(\theta_k - \alpha) \cdot \sin(\theta_k - \alpha) \\ -\cos(\theta_k - \alpha) \cdot \sin(\theta_k - \alpha) & \cos(\theta_k - \alpha) \cdot \sin(\theta_k - \alpha) & \cos(\theta_k - \alpha)^2 - \sin(\theta_k - \alpha)^2 \end{pmatrix}$$

$$A(\alpha) := \sum_k \left[T(k,\alpha)^{-1} \cdot Q(k) \cdot T(k,\alpha)^{-1^T} \cdot \left[\left(z_{k+1}\right) - \left(z_k\right) \right] \right]$$

$$A(0\cdot\text{deg}) = \begin{pmatrix} 4.304 \times 10^5 & 1.328 \times 10^5 & 9.649 \times 10^{-12} \\ 1.328 \times 10^5 & 4.304 \times 10^5 & -8.684 \times 10^{-11} \\ 9.649 \times 10^{-12} & -8.684 \times 10^{-11} & 1.488 \times 10^5 \end{pmatrix} \frac{\text{lb}}{\text{in}}$$

$$B(\alpha) := \frac{1}{2} \cdot \sum_k \left[T(k,\alpha)^{-1} \cdot Q(k) \cdot T(k,\alpha)^{-1^T} \cdot \left[\left(z_{k+1}\right)^2 - \left(z_k\right)^2 \right] \right]$$

$$B(0\cdot\text{deg}) = \begin{pmatrix} 4.523 \times 10^{-13} & 1.696 \times 10^{-13} & 5.654 \times 10^{-14} \\ 1.696 \times 10^{-13} & 6.784 \times 10^{-13} & 0 \\ -5.654 \times 10^{-14} & 0 & 2.12 \times 10^{-13} \end{pmatrix} \text{in} \cdot \frac{\text{lb}}{\text{in}}$$

$$D(\alpha) := \frac{1}{3} \cdot \sum_k \left[T(k,\alpha)^{-1} \cdot Q(k) \cdot T(k,\alpha)^{-1^T} \cdot \left[\left(z_{k+1}\right)^3 - \left(z_k\right)^3 \right] \right]$$

$$D(0\cdot\text{deg}) = \begin{pmatrix} 113.748 & 14.419 & 11.189 \\ 14.419 & 39.154 & 11.189 \\ 11.189 & 11.189 & 17.002 \end{pmatrix} \text{in} \cdot \text{lb}$$

$\theta^T = (0 \;\; 45 \;\; 90 \;\; -45 \;\; -45 \;\; 90 \;\; 45 \;\; 0)\,\text{deg}$

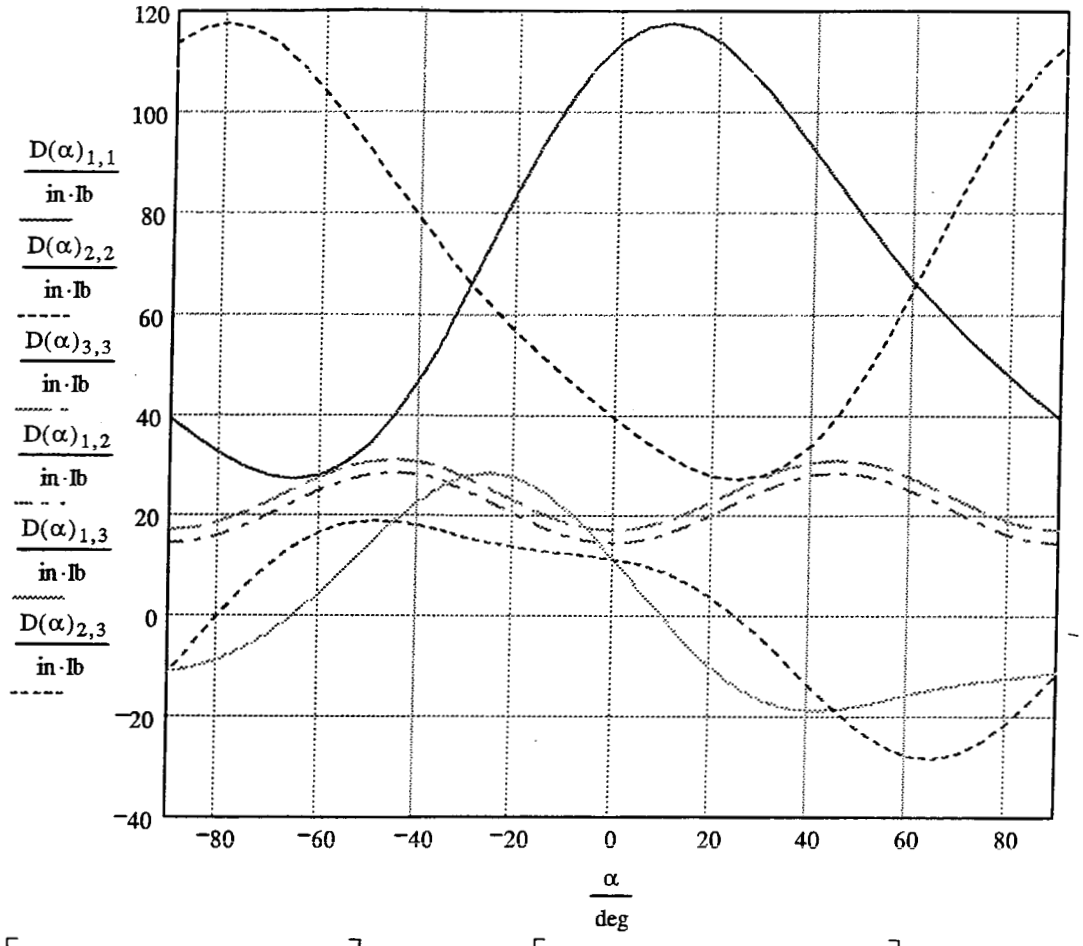

$\text{root}\left[\frac{d}{d\alpha}\left(D(\alpha)_{1,1}\right),\alpha,1\cdot\text{deg},90\cdot\text{deg}\right] = 9.6\,\text{deg}$ $\text{root}\left[\frac{d}{d\alpha}\left(D(\alpha)_{1,1}\right),\alpha,-90\cdot\text{deg},0\cdot\text{deg}\right] = -65.2\,\text{deg}$

$\text{root}\left[\frac{d}{d\alpha}\left(D(\alpha)_{2,2}\right),\alpha,-90\cdot\text{deg},-70\cdot\text{deg}\right] = -80.3$ $\text{root}\left[\frac{d}{d\alpha}\left(D(\alpha)_{2,2}\right),\alpha,0\cdot\text{deg},60\cdot\text{deg}\right] = 24.8\,\text{deg}$

$\text{root}\left[\frac{d}{d\alpha}\left(D(\alpha)_{3,3}\right),\alpha,0\cdot\text{deg},90\cdot\text{deg}\right] = 0\,\text{deg}$ $\text{root}\left[\frac{d}{d\alpha}\left(D(\alpha)_{3,3}\right),\alpha,-80\cdot\text{deg},-10\cdot\text{deg}\right] = -45\,\text{deg}$

$\text{root}\left[\frac{d}{d\alpha}\left(D(\alpha)_{1,2}\right),\alpha,0\cdot\text{deg},90\cdot\text{deg}\right] = 0\,\text{deg}$ $\text{root}\left[\frac{d}{d\alpha}\left(D(\alpha)_{1,2}\right),\alpha,-80\cdot\text{deg},-10\cdot\text{deg}\right] = -45\,\text{deg}$

$\text{root}\left[\frac{d}{d\alpha}\left(D(\alpha)_{1,3}\right),\alpha,0\cdot\text{deg},90\cdot\text{deg}\right] = 41.3\,\text{deg}$ $\text{root}\left[\frac{d}{d\alpha}\left(D(\alpha)_{1,3}\right),\alpha,-80\cdot\text{deg},-10\cdot\text{deg}\right] = -25.6\,\text{deg}$

$\text{root}\left[\frac{d}{d\alpha}\left(D(\alpha)_{2,3}\right),\alpha,0\cdot\text{deg},90\cdot\text{deg}\right] = 64.4\,\text{deg}$ $\text{root}\left[\frac{d}{d\alpha}\left(D(\alpha)_{2,3}\right),\alpha,-90\cdot\text{deg},0\cdot\text{deg}\right] = -48.7\,\text{deg}$

$\theta^T = (0 \;\; 45 \;\; 90 \;\; -45 \;\; -45 \;\; 90 \;\; 45 \;\; 0)\,\text{deg}$

$D(\alpha)_{1,1}$ in·lb

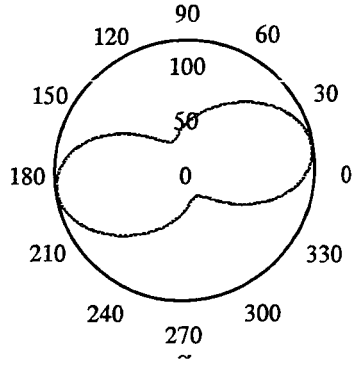

$D(\alpha)_{1,2}$ in·lb

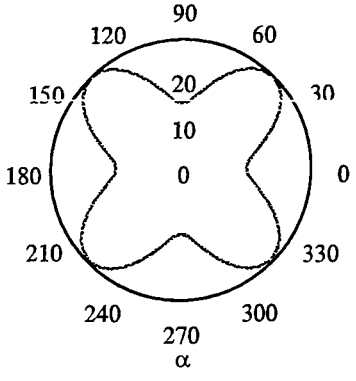

$D(\alpha)_{2,2}$ in·lb

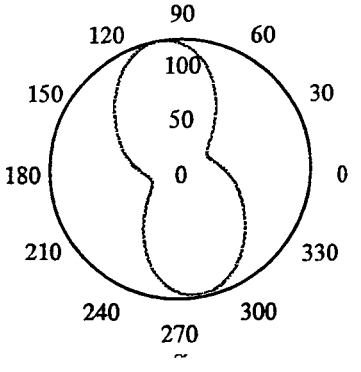

$D(\alpha)_{1,3}$ in·lb

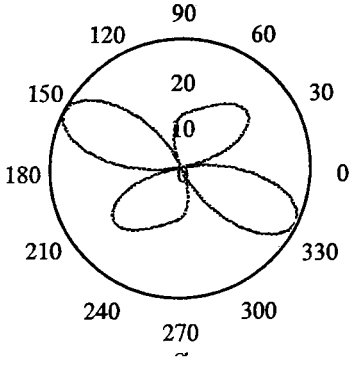

$D(\alpha)_{2,3}$ in·lb

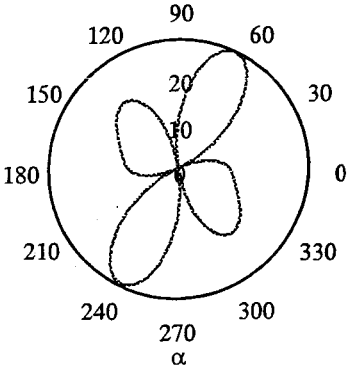

$D(\alpha)_{3,3}$ in·lb

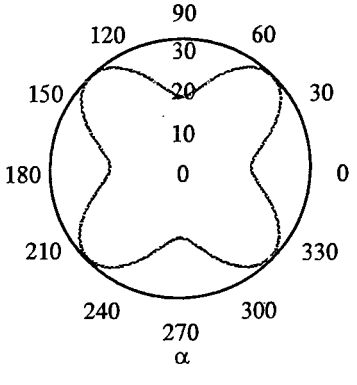

$D(\alpha)_{1,1}$ in·lb

$D(\alpha)_{2,2}$ in·lb

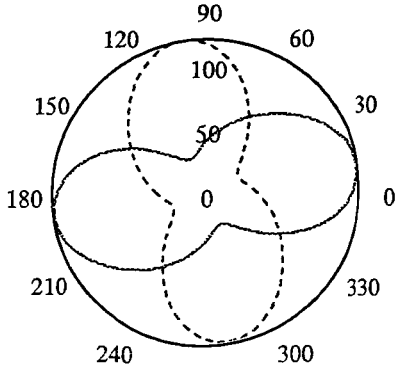

$D(\alpha)_{1,2}$ in·lb

$D(\alpha)_{2,3}$ in·lb

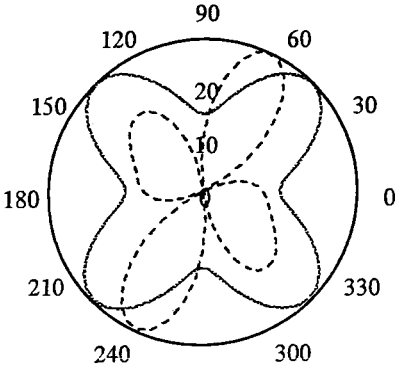

Invariants

$$U01_k := \frac{1}{8}\cdot\left(3\cdot Q11_k + 2\cdot Q12_k + 4\cdot Q66_k + 3\cdot Q22_k\right) \qquad U01_1 = 9.783\times 10^6 \text{ psi}$$

$$U02_k := \frac{1}{2}\cdot\left(Q11_k - Q22_k\right) \qquad U02_1 = 1.121\times 10^7 \text{ psi}$$

$$U03_k := \frac{1}{8}\cdot\left(Q11_k - 2\cdot Q12_k + Q22_k - 4\cdot Q66_k\right) \qquad U03_1 = 2.632\times 10^6 \text{ psi}$$

$$U04_k := \frac{1}{8}\cdot\left(Q11_k + 2\cdot Q12_k + Q22_k - 4\cdot Q66_k\right) \qquad U04_1 = 2.825\times 10^6 \text{ psi}$$

$$U05_k := \frac{1}{2}\cdot\left(-Q11_k + 2\cdot Q12_k - Q22_k + 16\cdot Q66_k\right) \qquad U05_1 = -6.029\times 10^6 \text{ psi}$$

$$U06_k := \frac{1}{4}\cdot\left(Q11_k - 2\cdot Q12_k + Q22_k\right) \qquad U06_1 = 6.014\times 10^6 \text{ psi}$$

$$U07_k := \frac{1}{16}\cdot\left(-Q11_k + Q12_k + 2\,Q66_k\right) \qquad U07_1 = -1.359\times 10^6 \text{ psi}$$

$$U08_k := \frac{1}{8}\left(Q12_k - Q22_k + 2\cdot Q66_k\right) \qquad U08_1 = 8.496\times 10^4 \text{ psi}$$

$$U09_k := \frac{1}{8}\cdot\left(Q11_k - 2\cdot Q12_k + Q22_k + 4\cdot Q66_k\right) \qquad U09_1 = 3.382\times 10^6 \text{ psi}$$

$$U10_k := \frac{1}{2}\cdot\left(Q11_k - 2\cdot Q12_k + Q22_k - 4\cdot Q66_k\right) \qquad U10_1 = 1.053\times 10^7 \text{ psi}$$

$$U11_k := \frac{1}{8}\cdot\left(-Q11_k - 2\cdot Q12_k + 3\cdot Q22_k - 4\cdot Q66_k\right) \qquad U11_1 = -2.972\times 10^6 \text{ psi}$$

$$U12_k := \frac{1}{4}\cdot\left(-Q11_k - 3\cdot Q12_k + 4\cdot Q22_k - 6\cdot Q66_k\right) \qquad U12_1 = -6.114\times 10^6 \text{ psi}$$

$$U13_k := \frac{1}{8}\cdot\left(-Q11_k + 6\cdot Q12_k - 5\cdot Q22_k + 12\cdot Q66_k\right) \qquad U13_1 = -2.292\times 10^6 \text{ psi}$$

$$U14_k := \frac{1}{8}\cdot\left(Q11_k - 4\cdot Q12_k + 4\cdot Q22_k - 10\cdot Q66_k\right) \qquad U14_1 = 2.426\times 10^6 \text{ psi}$$

$$U15_k := \frac{1}{8}\cdot\left(-Q11_k + 2\cdot Q12_k - Q22_k + 4\cdot Q66_k\right) \qquad U15_1 = -2.632\times 10^6 \text{ psi}$$

$$U16_k := \frac{-1}{8}\cdot Q12_k \qquad U16_1 = -4.825\times 10^4 \text{ psi}$$

$$\alpha := -180 \cdot deg, -175 \cdot deg .. 180 \cdot deg$$

$$D11(\alpha) := \frac{1}{3} \cdot \sum_{k=1}^{N} \left[\left(U01_k + U02_k \cdot \cos(2 \cdot \alpha) \cdot \cos(2 \cdot \theta_k) + U02_k \cdot \sin(2 \cdot \alpha) \cdot \sin(2 \cdot \theta_k) + U03_k \cdot \cos(4 \cdot \alpha) \cdot \cos(4 \cdot \theta_k \right.\right.$$

$$D12(\alpha) := \frac{1}{3} \cdot \sum_{k=1}^{N} \left[\left(U04_k - U04_k \cdot \cos(4 \cdot \alpha) \cdot \cos(4 \cdot \theta_k) + \frac{1}{4} \cdot U05_k \cdot \sin(4 \cdot \alpha) \cdot \sin(4 \cdot \theta_k) \right) \cdot \left[(z_{k+1})^3 - (z_k)^3 \right] \right]$$

$$D22(\alpha) := \frac{1}{3} \cdot \sum_{k=1}^{N} \left[\left(U01_k - U02_k \cdot \cos(2 \cdot \alpha) \cdot \cos(2 \cdot \theta_k) - U02_k \cdot \sin(2 \cdot \alpha) \cdot \sin(2 \cdot \theta_k) + U03_k \cdot \cos(4 \cdot \alpha) \cdot \cos(4 \cdot \theta \right.\right.$$

$$D26(\alpha) := \frac{1}{3} \cdot \sum_{k=1}^{N} \left[\left[\frac{1}{4} \cdot U11_k \cdot \sin(4 \cdot \alpha) + \frac{1}{2} \cdot U02_k \cdot \sin(2 \cdot \alpha) \cdot \cos(2 \cdot \theta_k) + U12_k \cdot \cos(2 \cdot \alpha) \cdot \sin(2 \cdot \theta_k) + \frac{1}{2} \cdot U13_k \right.\right.$$

$$D66(\alpha) := \frac{1}{3} \cdot \sum_{k=1}^{N} \left[\left(U09_k - U03_k \cdot \cos(4 \cdot \alpha) \cdot \cos(4 \cdot \theta_k) - \frac{1}{4} \cdot U10_k \cdot \sin(4 \cdot \alpha) \cdot \sin(4 \cdot \theta_k) \right) \cdot \left[(z_{k+1})^3 - (z_k)^3 \right] \right]$$

$$D16(\alpha) := \frac{1}{3} \cdot \sum_{k=1}^{N} \left[\left[\frac{1}{2} \cdot U02_k \cdot \sin(2 \cdot \alpha) \cdot \cos(2 \cdot \theta_k) - \frac{1}{4} U02_k \cdot \sin(2 \cdot \alpha) \cdot \sin(2 \cdot \theta_k) + U03_k \cdot \sin(4 \cdot \alpha) + \left[\frac{1}{4} \cdot U06_1 \right.\right.\right.$$

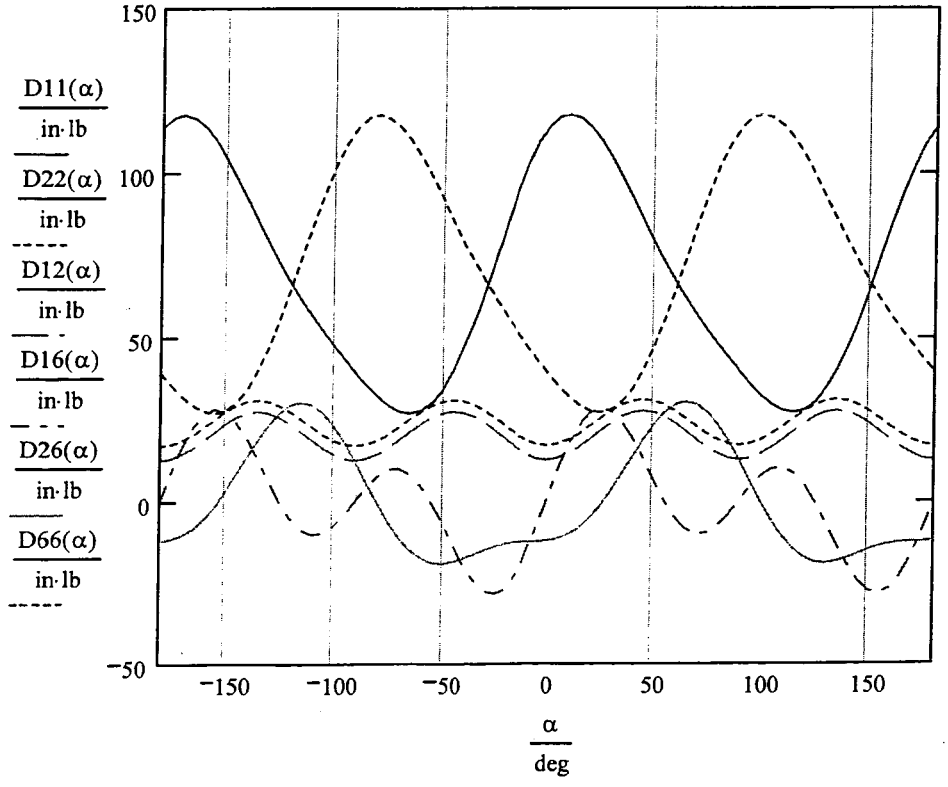

$$D(\alpha) := \begin{pmatrix} D11(\alpha) & D12(\alpha) & D16(\alpha) \\ D12(\alpha) & D22(\alpha) & D26(\alpha) \\ D16(\alpha) & D26(\alpha) & D66(\alpha) \end{pmatrix} \qquad D(0) = \begin{pmatrix} 113.748 & 12.535 & 0 \\ 12.535 & 39.154 & -12.207 \\ 0 & -12.207 & 17.002 \end{pmatrix} \text{ in·lb}$$

$$Eu_{norm}(\alpha) := \left[\sum_{i=1}^{3} \sum_{j=1}^{3} \left(D(\alpha)_{i,j} \right)^2 \right]^{\frac{1}{2}}$$

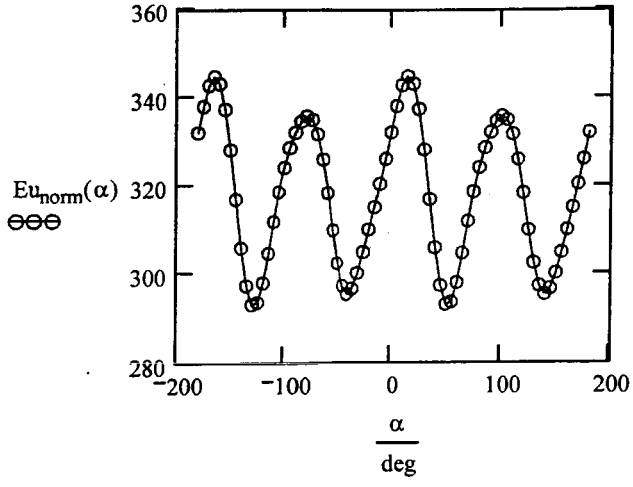

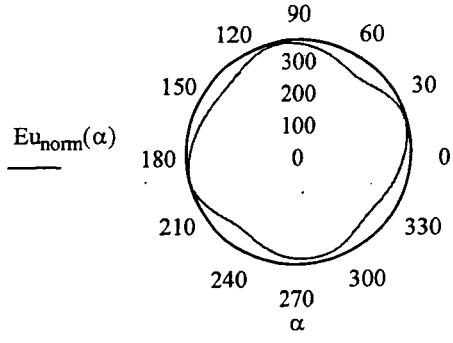

$\theta^T = (0 \;\; 45 \;\; 90 \;\; -45 \;\; -45 \;\; 90 \;\; 45 \;\; 0)\,\text{deg}$

D11(α)
in·lb

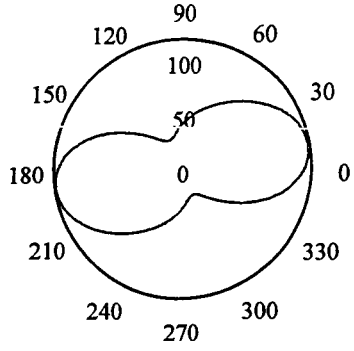

D12(α)
in·lb

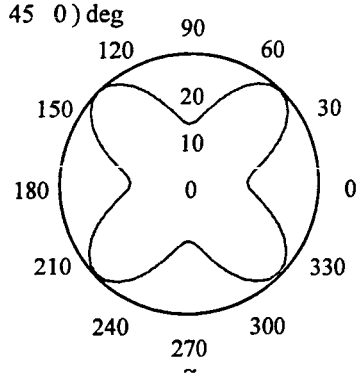

D22(α)
in·lb

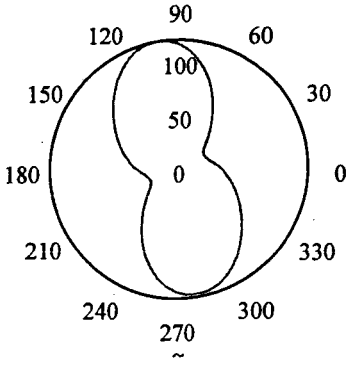

D16(α)
in·lb

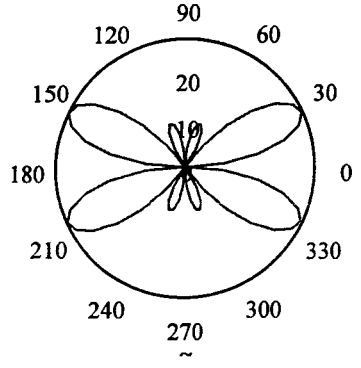

D26(α)
in·lb

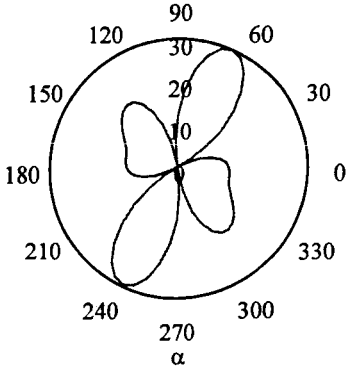

D66(α)
in·lb

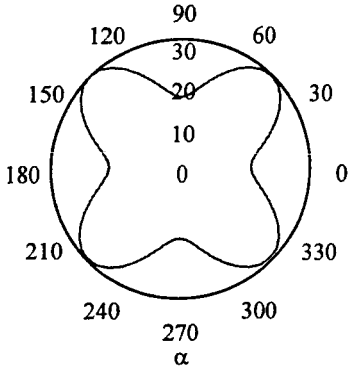

D11(α)
in·lb

D22(α)
in·lb

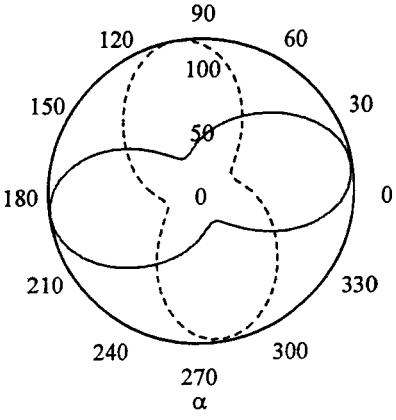

D12(α)
in·lb

D26(α)
in·lb

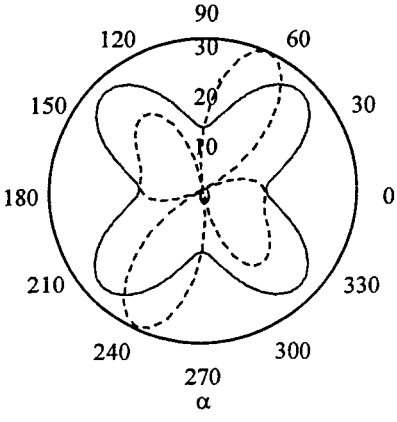

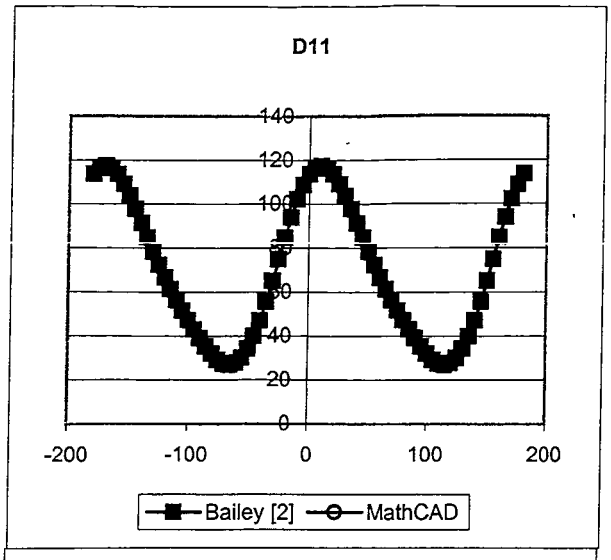

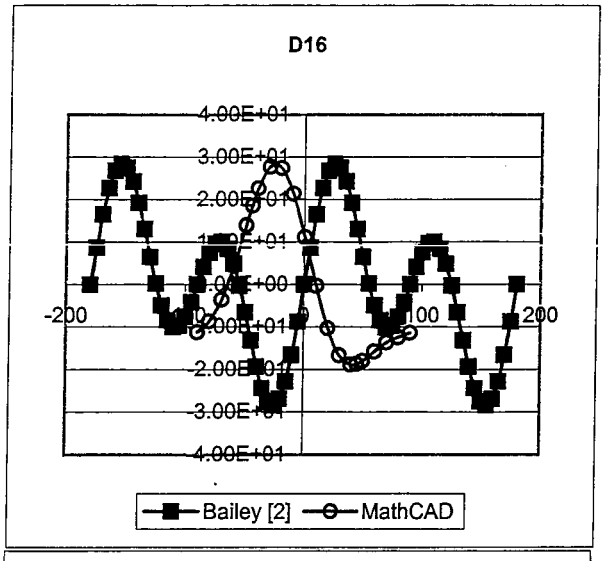

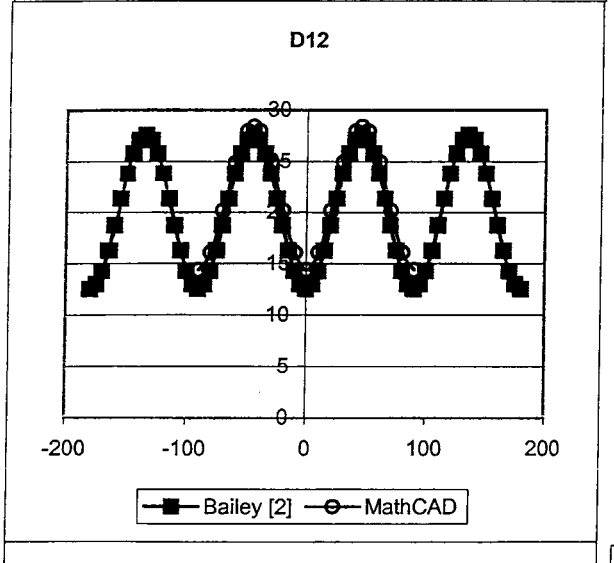

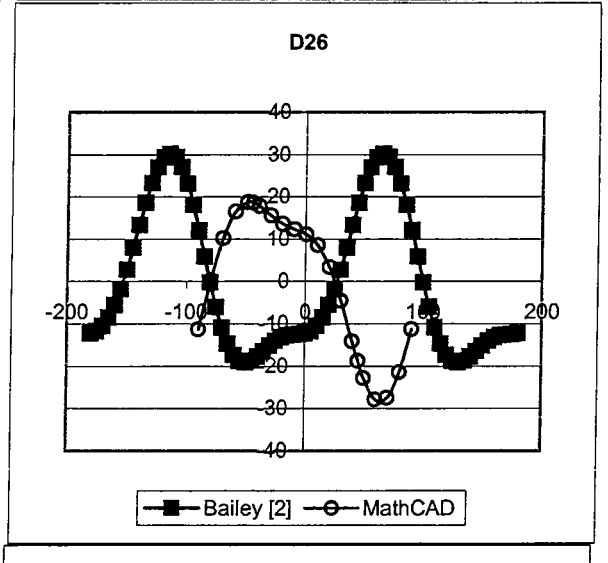

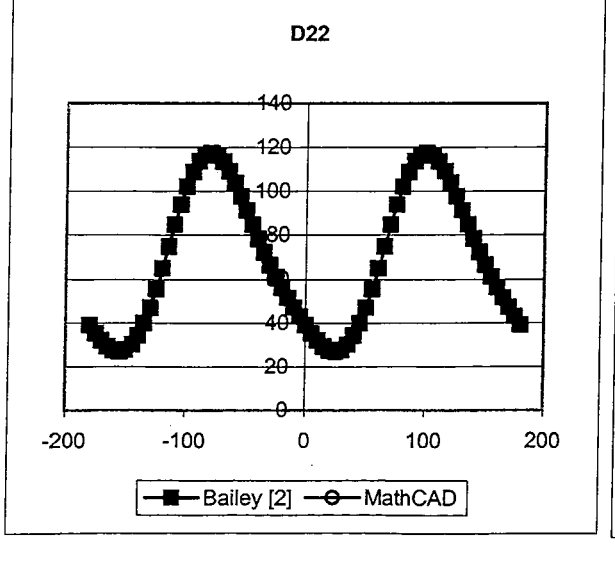

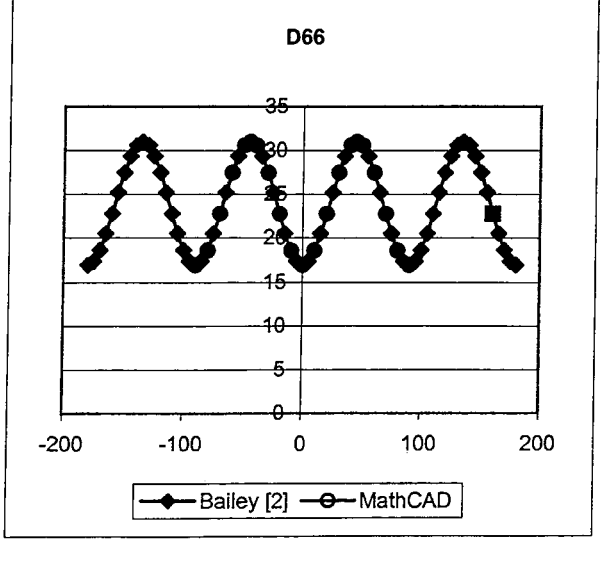

D matrix using Patran and modifying laminate versus Bailey's usage of invarients

```
ASSIGN OUTPUT2 = 'disk_20_360_RT.op2', UNIT = 12
SOL 106
TIME 600
CEND
TEMP(INIT)=1
SUBCASE 1
$ Subcase name : Assembly
   SUBTITLE=Assembly
   NLPARM = 1
   SPC = 2
   LOAD = 2
   TEMPERATURE(LOAD) = 70
   DISPLACEMENT(PLOT,SORT1,REAL)=ALL
   SPCFORCES(PLOT,SORT1,REAL)=ALL
   STRAIN(PLOT,SORT1,REAL,VONMISES,FIBER,CENTER)=ALL
   STRESS(PLOT,SORT1,REAL,VONMISES,CENTER)=ALL
   FORCE(PLOT,SORT1,REAL,CENTER)=ALL
SUBCASE 2
$ Subcase name : Assem_Press@RT
   SUBTITLE=Assem_Press@RT
   NLPARM = 2
   SPC = 2
   LOAD = 4
   TEMPERATURE(LOAD) = 70
   DISPLACEMENT(PLOT,SORT1,REAL)=ALL
   SPCFORCES(PLOT,SORT1,REAL)=ALL
   STRAIN(PLOT,SORT1,REAL,VONMISES,FIBER,CENTER)=ALL
   STRESS(PLOT,SORT1,REAL,VONMISES,CENTER)=ALL
   FORCE(PLOT,SORT1,REAL,CENTER)=ALL
BEGIN BULK
PARAM     POST     -1
PARAM     WTMASS   .00259
PARAM     GRDPNT   0
PARAM     LGDISP   1
PARAM,NOCOMPS,0
PARAM    PRTMAXIM YES
NLPARM    1        10               AUTO     5        25       UPW      YES
          .001     .001     1.-7
NLPARM    2        12               AUTO     5        25       UPW      YES
          .001     .001     1.-7
$ Direct Text Input for Bulk Data
TEMPD,1,70.
TEMPD,70,70.
PCOMP     1                                                    70.      0.
          8552     .0055    0.       YES      8552     .0055    45.      YES
          8552     .0055    90.      YES      8552     .0055   -45.      YES
          8552     .0055   -45.      YES      8552     .0055    90.      YES
          8552     .0055    45.      YES      8552     .0055    0.       YES
$ Referenced Material Records
$ Material Record : Invar
$ Description of Material : Date: 02-Aug-01           Time: 15:17:17
MAT1      1        2.15+7           .25              9.-7     260.
$ Material Record : IM7.8552_RT
$ Description of Material : Date: 30-Jul-01           Time: 15:15:33
MAT8      8552     2.35+7   1.2+6   .32      750000. 750000. 750000. .06
         -3.-7     1.5-5    70.     310000. 106000. 10400.  44000.  15000.
$
```